

UNIVERSITY OF GRONINGEN

BACHELOR THESIS

Investigating the AGN/starburst composite APM 08279+5255 at redshift 4

Author:
Roland TIMMERMAN

Supervisor:
Dr. John P. MCKEAN

July 7, 2017



Abstract

In this thesis I present new JVLA data of the quasar APM08279+5255. The goal of this thesis is to find if the CO($J = 1 \rightarrow 0$) emission can be resolved on 100 mas scales, and to determine whether AGN or star-formation activity is responsible for the continuum emission at an observed frequency of 23.9 GHz. First, I present the basics of active galactic nuclei, radio emission mechanics, and interferometry. After that, I explain the calibration procedure, followed by the results of the new JVLA data, and a discussion of the results. In summary, I find that the continuum emission shows a dominant unresolved component and a weak extended component, and I derive a total flux density of the quasar of $406 \pm 22 \mu\text{Jy}$. Also, I find that the CO($J = 1 \rightarrow 0$) emission has an unresolved component coincident with the peaks in the continuum maps, as well as additional structure to the west which may be related to AGN outflow. I also find evidence suggesting that time variability in the peak brightness of each of the gravitationally lensed images may exist on the order of days. Finally, I conclude that AGN-related activity is the most likely explanation for the continuum emission at an observed frequency of 23.9 GHz.

Acknowledgements

While a Bachelor thesis is only a relatively small first step in one's academic career, it is still something to be proud of. However, I could not have done it all by myself. I'd like to thank Dr. John McKean for being a very knowledgeable, patient, passionate and helpful supervisor. He did not hesitate to take all the time that was needed to explain the matter to me, even at the most inconvenient moments (like right before lunch, or at 5 pm). When showing my results to him, he was probably even more enthusiastic as I was, although this is probably just because he understood the scientific relevance much better than I did.

Also, I'd like to thank Cristiana Spingola and Hannah Stacey (alphabetical order) for always helping me out whenever John wasn't around. Their knowledge of the topic was very useful, and they were able to help me out with practically every question I had.

Next, I'd like to thank Kevin Bixerman and Daniël Koot for the fruitful discussions we had, and for being great company during this project.

Last, but definitely not least, I'd like to thank my parents for their great support for me these last three years. I really couldn't have done it without them.

Contents

Acknowledgements	1
1 Introduction	3
1.1 APM08279+5255	3
1.2 Previous research	3
1.3 Motivation for this thesis	4
2 Theory	5
2.1 Active Galactic Nuclei	5
2.2 Emission Mechanisms	6
2.2.1 Synchrotron emission	6
2.2.2 Free-free emission	8
2.3 Interferometry	11
2.4 Jansky Very Large Array	14
3 Data Reduction	15
3.1 Observations	15
3.2 Calibration	15
3.3 Imaging	20
4 Results	21
4.1 Dataset summary	21
4.2 Continuum emission	21
4.3 CO($J = 1 \rightarrow 0$)	25
4.4 Time variations	27
4.5 Wide-field imaging	29
5 Discussion	30
5.1 Continuum imaging	30
5.2 CO($J = 1 \rightarrow 0$)	31
5.3 Time variations	33
5.4 Wide-field imaging	33
5.5 Identifying the cause of radio emission	34
6 Conclusion	35
Bibliography	36
A Images of observations	37
B Python code	41

Chapter 1

Introduction

1.1 APM08279+5255

APM08279+5255 is a strongly lensed radio-quiet broad absorption line quasar at a redshift of 3.911 (Riechers et al., 2009). It was recognized to be a quasar by Irwin et al. (1998), though it has been observed earlier thanks to its high brightness. A month later, the first evidence for the gravitational lensing of APM08279+5255 was given by Ledoux et al. (1998) by resolving the quasar into two images. Subsequent research by Ibata et al. (1999) using the NICMOS high-resolution camera on board the Hubble Space Telescope revealed a third image, as shown in Figure 1.1. It was shown by Lewis et al. (2002) using data taken with the STIS spectrograph that these images are in fact gravitationally lensed images of the same quasar, and not just three sources that happen to be nearby one another.

1.2 Previous research

In 2009, Riechers et al. used Very large Array (VLA) data taken in B, C, and D configuration to investigate the $\text{CO}(J = 1 \rightarrow 0)$ line in APM08279+5255. They found the $\text{CO}(J = 1 \rightarrow 0)$ emission to be resolved with a lensed source size of approximately $0.3''$, as shown in Figure 1.2. Also, they find that the continuum emission around the $\text{CO}(J = 1 \rightarrow 0)$ line is slightly more extended. The $\text{CO}(J = 1 \rightarrow 0)$ emission is reported to be located in three images, two of which are blended together. They did not find evidence for extended $\text{CO}(J = 1 \rightarrow 0)$ emission on arcsecond scales. They also report the detection of a radio source $3''$ south of APM08279+5255, but they do not think that it is related to the quasar. They were not able to find this radio source at a frequency of 23.5 GHz. Based on the SED, they find that the quasar lies on the FIR-radio correlation, but since the Condon model does not give a reasonable fit for the SED, they find that star formation is not a likely cause of the radio continuum. Finally, they propose a new lens model for APM08279+5255 with a magnification of 4.2, where they assume a highly inclined elliptical lens, as shown in Figure 1.3.

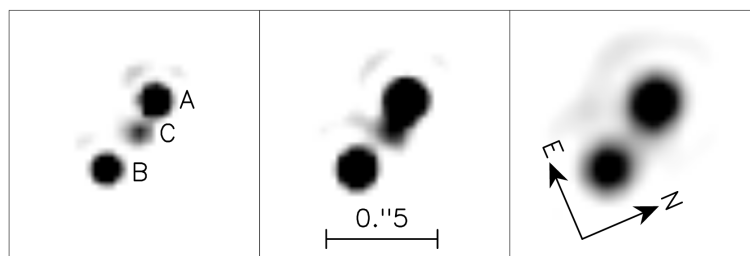


FIGURE 1.1: NICMOS image of APM08279+5255 through different filters. (Ibata et al., 1999)

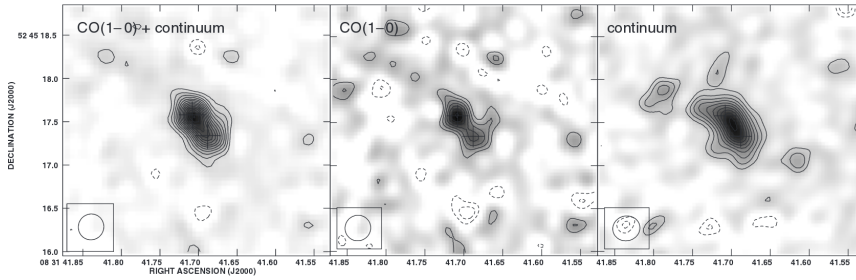


FIGURE 1.2: Image of the continuum emission and CO($J = 1 \rightarrow 0$) emission. (Riechers et al., 2009)

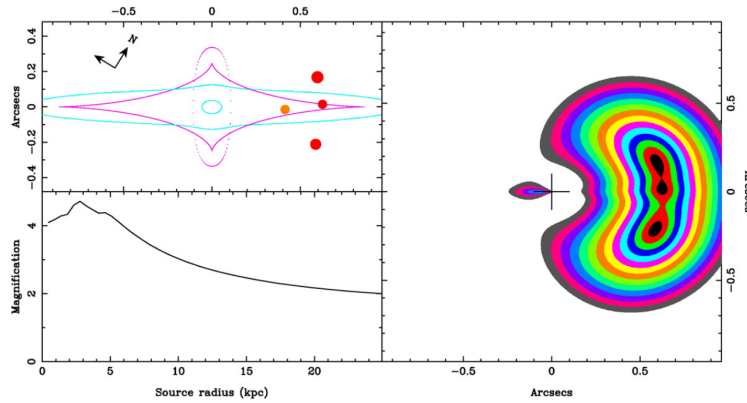


FIGURE 1.3: Model for the gravitational lens of APM08279+5255 by Riechers et al. (2009)

1.3 Motivation for this thesis

The relation between star formation and active galactic nuclei in the earliest galaxies is not yet fully understood. There are several models which describe the evolution of a quasar. Therefore it is important to gather data on these earliest galaxies.

In this thesis, I will use new high-resolution data from the Jansky Very Large Array (JVLA) to investigate the continuum emission and the CO($J = 1 \rightarrow 0$) emission of APM08279+5255. Whereas Riechers et al. used narrow-band VLA data in B, C and D configuration, we have broad-band JVLA data in A-configuration, This allows us to separate the CO($J = 1 \rightarrow 0$) emission from the continuum emission much better, and it allows for much better angular resolution. In order to try to find evidence for AGN-related emission, I will make a high-resolution map of the continuum and CO($J = 1 \rightarrow 0$) emission and investigate the possibility of time variations in the flux density of the quasar at 23.9 GHz. Finally, I will make a wide-field image of the environment of APM08279+5255 to check if there is any evidence for molecular gas or continuum emission surrounding the quasar on large scales. This wide-field image will also be used to check for the unknown radio source $3''$ south of APM08279+5255.

Chapter 2

Theory

In order to understand the work done in this thesis, it is important to know about the type of object that is being studied, the emission mechanisms that allow us to observe the object, and the techniques used to observe it. Therefore, a brief overview of those topics is given below.

2.1 Active Galactic Nuclei

In the center of some galaxies it is possible to find an extraordinary amount of activity. These galactic centers are called "Active Galactic Nuclei" or AGN for that very reason. There are several types of active galactic nuclei, but in essence they are very similar. The current models describe active galactic nuclei as a super massive black hole that is accreting large amounts of matter in the center of a galaxy. As the matter approaches the black hole, its sideways motion prevents it from directly falling into the black hole. Instead, it forms an accretion disk. Due to the strong force of gravity, the inflowing matter is compressed up to extremely high temperatures. This causes it to emit radiation. Depending on the angle between the line of sight and the accretion disk, this emission can be blocked. Additionally, the magnetic field surrounding the rotating black hole can cause jets of matter to be emitted from the AGN at relativistic speeds. These jets can travel for several thousand lightyears before the intergalactic medium slowly brings it to a halt, creating two large lobes of plasma on either side of the AGN. An example of this is shown in Figure 2.1.

In rare cases, the AGN can so bright that it out-shines the rest of its host galaxy. This causes the galaxy to appear like a point source. These types of AGN are called quasi-stellar objects, or *quasars* for short.

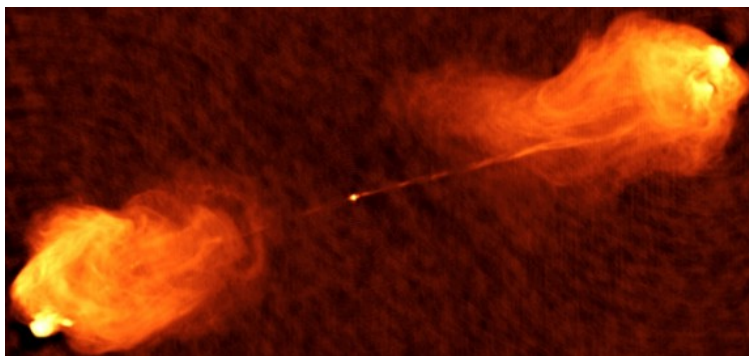


FIGURE 2.1: Radio image of Cygnus A showing the relativistic jets
(Image by NRAO)

2.2 Emission Mechanisms

Since it is one of the main goals of this thesis to find out whether the emission of APM08279+5255 at a rest frequency of 115 GHz is caused by star-formation or the AGN, it is important to know about two emission mechanisms: synchrotron radiation and free-free emission. These two emission mechanisms dominate the radio spectrum, and it is by studying this spectrum that we can learn about what causes the continuum emission of the quasar. An example of a radio continuum spectrum is shown in Figure 2.2. The slope to the left of the spectral energy distribution is the synchrotron radiation. In the middle of the plot, the flat line shows the free-free emission component. To the right is the thermal emission, which covers most of the infrared and optical part of the spectrum. The data that we use in this thesis is measured at a frequency of about 24 GHz. That means that the data gives us insight into the narrow part of the spectrum where both synchrotron radiation and free-free emission can play a role. In addition, since we have a bandwidth of 2 GHz, we may be able to get an idea of what the slope of the spectrum is at that point.

In the following two paragraphs a basic overview of the two main emission mechanisms is given. For a more detailed explanation, see Condon et al. (2016).

2.2.1 Synchrotron emission

One of the basic equations of electromagnetism is the equation for force on a charged particle due to a magnetic field:

$$\vec{F} = q(\vec{v} \times \vec{B}) \quad (2.1)$$

where \vec{F} is the force on the particle, q is its charge, \vec{v} is the velocity of the particle and \vec{B} is the magnetic field. Since the force on the particle is perpendicular to its velocity, it will follow a spiral trajectory. The frequency of this spiral motion can be calculated by equating the centripetal force to the magnetic force. This gives the gyro frequency:

$$\omega_G = 2\pi\nu_G = \frac{eB}{m_e c} \quad (2.2)$$

where e is the charge of an electron, m_e is the mass on an electron, and c is the speed

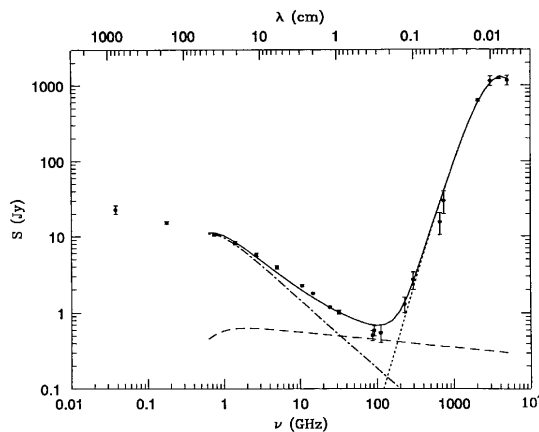


FIGURE 2.2: Spectral energy distribution of M82. Image credit: NRAO

of light. This means that the particle is able to maintain speed relatively well, while being accelerated constantly. Due to this acceleration, the particle will emit radiation. Ofcourse, this radiation costs energy which will slow the particle down eventually. At low velocities, this radiation is called *cyclotron radiation*, but at relativistic velocities it is called *synchrotron radiation*. The power emitted by the acceleration of an electron can be calculated using the relativistic Larmor formula:

$$P = \frac{2e^2}{3c^3} \gamma^4 a^2 \quad (2.3)$$

where P is the power, γ is the Lorentz factor, and a is the acceleration of the particle. By taking the acceleration to be the acceleration due to the magnetic field, we can get that the power emitted by an electron due to the magnetic field is as following:

$$P = \frac{2e^2}{3c^3} \gamma^2 \frac{e^2 B^2}{m_e^2 c^2} v^2 \sin^2 \alpha = 2\sigma_T \beta^2 \gamma^2 c U_B \sin^2 \alpha \quad (2.4)$$

where α is the angle between the velocity and the magnetic field, σ_T is the Thompson cross section as defined by $\sigma_T \equiv 8\pi(e^2/m_e c^2)^2/3$, and U_B is the magnetic energy density defined by $U_B \equiv B^2/8\pi$. Averaging this over all pitch angles gives the average power emitted:

$$\langle P \rangle = \frac{4}{3} \sigma_T \beta^2 \gamma^2 c U_B. \quad (2.5)$$

The frequency dependence of the synchrotron power is given by

$$P(\nu) = \sqrt{3} \frac{e^3 B \sin \alpha}{m_e c^2} \left(\frac{\nu}{\nu_c} \right) \int_{\nu/\nu_c}^{\infty} K_{5/3}(\eta) d\eta \quad (2.6)$$

where $K_{5/3}$ is a modified Bessel function and the critical frequency ν_c is given by

$$\nu_c = \frac{3}{4\pi} \frac{e \gamma^2 B}{m_e c} \sin \alpha = \frac{3}{2} \gamma^2 \nu_G \sin \alpha \quad (2.7)$$

The energy distribution of electrons in our galaxy follows a power law:

$$N(E)dE = K E^{-\delta} dE \quad (2.8)$$

where $N(E)dE$ is the amount of electrons with an energy between E and $E + dE$, K is a constant, δ is a power-law index, and dE is an infinitesimal range of energy. Assuming that the electrons emit away their energy at a frequency of

$$\nu \approx \gamma^2 \nu_G \quad (2.9)$$

and with an emission coefficient of

$$\epsilon_\nu d\nu = -\frac{dE}{dt} N(E) dE. \quad (2.10)$$

we can write the energy as

$$E = \gamma m_e c^2 \approx \left(\frac{\nu}{\nu_G} \right)^{1/2} m_e c^2. \quad (2.11)$$

Taking the derivative of this with respect to frequency gives

$$\frac{dE}{d\nu} \approx \frac{m_e c^2 \nu^{-1/2}}{2\nu_G^{1/2}}. \quad (2.12)$$

Therefore, we find for the emission coefficient:

$$\epsilon_\nu \approx \left(\frac{4}{3} \sigma_T \beta^2 \gamma^2 c U_B \right) (K E^{-\delta}) \frac{m_e c^2 \nu^{-1/2}}{2 \nu_G^{1/2}}. \quad (2.13)$$

Taking only the dependence on ν and B (recall that $\nu_G \propto B$), we find

$$\epsilon_\nu \propto B^{(\delta+1)/2} \nu^{(1-\delta)/2}. \quad (2.14)$$

Finally, since the emission coefficient is proportional to the intensity of the radiation, we find that the spectral energy distribution of synchrotron radiation also follows a power law:

$$S_\nu \propto \nu^\alpha \quad (2.15)$$

where $\alpha = (1 - \delta)/2$. Typical values for α are between -0.4 and -1.2.

At low frequencies, synchrotron radiation deviates from this power-law due to *synchrotron self-absorption*. This is the re-absorption of emitted photons by the electrons. As the brightness temperature of the plasma becomes to high, it will get limited by the characteristic thermal temperature of the plasma. Since the effective temperature of the plasma can be written as

$$T_e = \frac{E}{3k_B} = \frac{\gamma m_e c^2}{3k_B} \propto \nu^{1/2} \quad (2.16)$$

where k_B is Boltzmann's constant, we find that the specific intensity becomes

$$I_\nu = \frac{2k_B \nu^2 T_b}{c^2} \propto \nu^{5/2}. \quad (2.17)$$

Therefore, synchrotron self-absorption causes a spectral index of 5/2 in the low-frequency regime.

Synchrotron radiation plays an important role in astrophysics because it can be emitted by active galactic nuclei and star-formation activity. In the case of an AGN, synchrotron radiation generally comes from the relativistic jets that can be emitted from either side of the AGN. If the AGN does not emit jets however, there will be no synchrotron radiation.

In the case of star-formation, synchrotron radiation is emitted through supernova remnants. Supernova remnants are associated with star-formation, and the shock waves of supernovae produce very large magnetic fields. Cosmic ray electrons can then interact with these magnetic fields to emit synchrotron radiation.

2.2.2 Free-free emission

Again, we start with one of the basic equations of electromagnetism: Coulomb's law.

$$\vec{F} = k_e \frac{q_1 q_2}{r^2} \hat{r} \quad (2.18)$$

where \vec{F} is the force between two charged particles, k_e is Coulomb's constant, q_1 and q_2 are the charges of the two charged particles, and r is the distance separating the two charges. This law states that two charges either attract or repel each other depending on their charges. Again, we can apply Larmor's formula to derive the

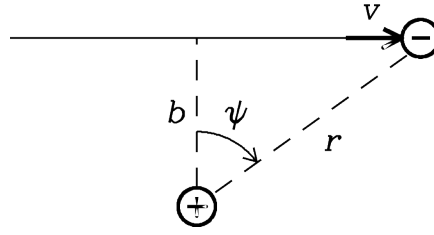


FIGURE 2.3: Schematic image of two charged particles passing one another (Condon et al., 2016).

power emitted due to this acceleration of charged particles.

Consider two particles: an electron and an ion. The electron has a charge e and the ion has a charge Ze . For simplicity, we assume that the ion is stationary. After all, we can always pick a reference frame where this is true. Assume that the velocity with which one particle passes the other is \vec{v} and the minimal distance between the two is the impact parameter b . Furthermore, we have a distance between the two particles of r , and we can define an angle ψ as shown in Figure 2.3.

As the electron passes the ion, they experience a force. This force can be decomposed into two components: one component parallel to its path, and one component perpendicular to its path. As it turns out, the parallel component generally causes infrared emission, so it's not of importance for this thesis.

We can write the perpendicular component of the force as following:

$$F_{\perp} = \frac{Ze^2}{r^2} \cos \psi = \frac{Ze^2 \cos^3 \psi}{b^2}. \quad (2.19)$$

Applying Larmor's formula gives:

$$P = \frac{2}{3} \frac{e^2 a_{\perp}^2}{c^3} = \frac{2}{3} \frac{Z^2 e^6}{m_e^2 c^3} \left(\frac{\cos^3 \psi}{b^2} \right)^2. \quad (2.20)$$

In order to get the total energy lost per interaction, we integrate this power over time. With the assumption that the interaction is not too strong, we find that the velocity remains relatively constant. This gives the following for the total emitted energy:

$$W = \frac{\pi}{4} \frac{Z^2 e^6}{m_e^2 c^3 b^3} \frac{1}{v}. \quad (2.21)$$

We can estimate the interaction length as $\tau \approx b/v$, which gives a frequency of $\nu_{max} \approx v/2\pi b$. We can approximate that the power spectrum is flat for all frequencies smaller than ν_{max} . In reality, we would need a Fourier transform, but that would just add unnecessary complexity. In this approximation, the average energy per unit frequency for a single interaction can be written as

$$W_{\nu} = \frac{W}{\nu_{max}} = \frac{\pi^2}{2} \frac{Z^2 e^6}{c^3 m_e^2} \left(\frac{1}{b^2 v^2} \right). \quad (2.22)$$

Now we need to find the distributions of the velocities and the impact parameters to determine the free-free emission spectrum. Since in local thermodynamic equilibrium the kinetic energies of both electrons and ions are the same, while ions are

much heavier, we can approximate that the velocities of the ions are negligible. The amount of interactions between electrons and ions with a velocity between v and dv , and an impact parameter between b and db per unit volume is then given by

$$N(v, b)dv db = (2\pi b db)(vf(v)dv)N_e N_i \quad (2.23)$$

where $vf(v)$ is the velocity distribution of the electrons, N_e is the number density of electrons, and N_i is the number density of ions. We can now define the emission coefficient at a frequency ν as the power emitted per steradian within a certain volume due to free-free emission:

$$\begin{aligned} 4\pi\epsilon_\nu &= \int_{b=0}^{\infty} \int_{v=0}^{\infty} W_\nu(v, b)N(v, b) dv db \\ &= \frac{\pi^3 Z^2 e^6 N_e N_i}{c^3 m_e^2} \int_{b=0}^{\infty} \frac{db}{b} \int_{v=0}^{\infty} \frac{f(v)}{v} dv. \end{aligned} \quad (2.24)$$

In order to solve these last integrals, we assume a non-relativistic Maxwellian velocity distribution, and we state that there is some minimum and maximum value for the impact parameter. There is a minimum value of the impact parameter because there is a maximum to the amount of momentum that can be transferred, and there is a maximum value of the impact parameter because the interaction becomes too weak to emit any significant radiation if the impact parameter becomes too large. The minimum value for the impact parameter is such that twice the initial momentum of the electron is transferred. There is also a quantum mechanical lower limit for the impact parameter due to Heisenberg's Uncertainty Principle, but it is generally lower than the classical limit, so it is ignored for now.

Filling in the non-relativistic Maxwellian velocity distribution gives

$$\int_{v=0}^{\infty} \frac{f(v)}{v} dv = \frac{4}{\sqrt{\pi}} \left(\frac{m_e}{2kT} \right)^{3/2} \int_{u=0}^{\infty} \frac{kT}{m_e} e^{-u} du = \left(\frac{2m_e}{\pi kT} \right)^{1/2} \quad (2.25)$$

where u is defined as $m_e v^2 / 2kT$. Using this, and the minimum and maximum values for the impact parameter, the emission coefficient becomes

$$\epsilon_\nu = \frac{\pi^2 Z^2 e^6 N_e N_i}{4c^3 m_e^2} \left(\frac{2m_e}{\pi kT} \right)^{1/2} \ln \left(\frac{b_{max}}{b_{min}} \right). \quad (2.26)$$

The minimum and maximum impact parameters are as following:

$$b_{min} = \frac{Ze^2}{m_e v^2}, \quad b_{max} = \frac{v}{2\pi\nu}. \quad (2.27)$$

Since we're assuming local thermodynamic equilibrium, the absorption coefficient can be calculated using Kirchoff's Law and the Reyleigh-Jeans limit of the blackbody brightness:

$$\kappa_\nu = \frac{\epsilon_\nu}{B_\nu(T)} = \frac{\epsilon_\nu c^2}{2kT\nu^2} \propto \frac{N_e N_i}{\nu^2 T^{3/2}} \ln \left(\frac{b_{max}}{b_{min}} \right). \quad (2.28)$$

Since b_{max} depends on the frequency, the absorption coefficient does not perfectly scale like $\kappa_\nu \propto \nu^{-2}$, but rather like $\kappa_\nu \propto \nu^{-2.1}$.

As a final step, the optical depth of the emitting region is of importance. The optical depth τ_ν can be calculated as

$$\tau_\nu = - \int \kappa_\nu ds \propto \int \frac{N_e N_i}{\nu^{2.1} T^{3/2}} ds. \quad (2.29)$$

The spectral energy distribution is now simply

$$S_\nu = (1 - e^{-\tau_\nu})B_\nu(T)\Delta\Omega. \quad (2.30)$$

If the emitting region is optically thick ($\tau \gg 1$), then the spectrum is like a blackbody:

$$S_\nu \propto \nu^2, \quad (2.31)$$

while if the emitting region is optically thin ($\tau \ll 1$), then we can approximate $1 - e^{-\tau}$ as τ , which gives

$$S_\nu \propto \tau_\nu \frac{2kT\nu^2}{c^2} \propto \nu^{-0.1}. \quad (2.32)$$

Free-free emission is generally associated with the hot environment of an AGN or with the HII regions that surround hot young stars. Since very hot stars only live briefly, the free-free emission from such regions can trace the star formation rate very well.

2.3 Interferometry

In order to understand what kind of data is used in this thesis and how the target source is observed, it is important to know about interferometry. This is a brief overview of the basics of interferometry. For a more detailed description, see Condon et al. (2016).

Radio telescopes use antennas to focus electromagnetic radiation on a receiver. This radiation induces a small voltage in the receiver, and this voltage can be measured to find the intensity of the incoming radiation. The wave nature of light, combined with the finite aperture of the telescope, causes the electromagnetic waves to be diffracted, which results in point sources on the sky being spread out. How point sources spread out is described by the point-spread function (PSF). This diffraction of light means that two nearby point sources on the sky can not be distinguished if their point spread functions start to overlap. How close two point sources can be before they become indistinguishable is called the angular resolution of the telescope, and can be calculated as

$$\theta = \alpha \frac{\lambda}{D} \quad (2.33)$$

where α is a dimensionless constant determined by the aperture illumination pattern (generally taken to be 1.22 for a Gaussian illumination pattern), λ is the wavelength of the electromagnetic waves, and D is the diameter of the antenna.

In order to improve the resolution of a telescope at a certain wavelength, there is only one option: increasing the diameter. However, building larger telescopes quickly becomes very difficult. The solution to this problem is to not improve the resolution of a single telescope, but to link multiple telescopes together. Instead of having a resolution dependent on the diameter of a single telescope, the resolution will depend on the separation between the telescopes:

$$\theta = \alpha \frac{\lambda}{B} \quad (2.34)$$

where B is the baseline (\sim separation) of two telescopes.

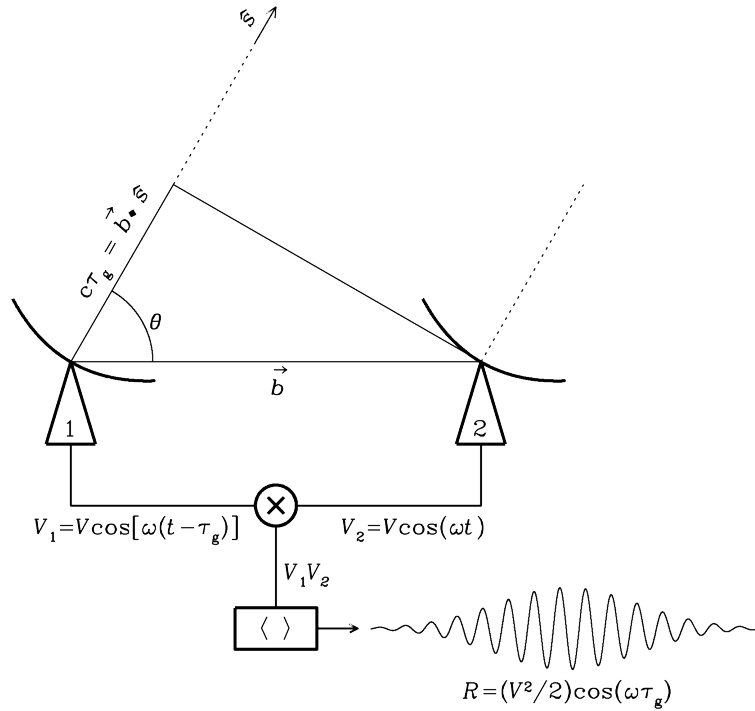


FIGURE 2.4: Block diagram of a two-element interferometer (Condon et al., 2016).

To explain how interferometers work, I'll consider a simple two-element interferometer, as shown in Figure 2.4.

This two-element interferometer consists of two radio telescopes, both pointed in the same direction. As is visible in Figure 2.4, the path length of electromagnetic waves is longer for one antenna than the other. The corresponding time difference (geometric delay) can be calculated as

$$\tau_g = \frac{\vec{b} \cdot \hat{s}}{c} \quad (2.35)$$

where \vec{b} is the baseline vector, \hat{s} is the direction unit vector and c is the speed of light. This means that the output voltage from each of the radio telescopes can be written as

$$V_1(t) = V \cos[\omega(t - \tau_g)], \quad V_2(t) = V \cos(\omega t) \quad (2.36)$$

where V is the amplitude voltage, ω is the angular frequency of the incoming radiation and t is the time. The correlator then digitally multiplies these voltages together to give

$$V_1 V_2 = \left(\frac{V^2}{2}\right) [\cos(2\omega t - \omega\tau_g) + \cos(\omega\tau_g)]. \quad (2.37)$$

The correlator then time-averages this signal, to remove the $\cos(2\omega t - \omega\tau_g)$ term. This gives the final response as

$$R = \frac{V^2}{2} \cos(\omega\tau_g). \quad (2.38)$$

This output depends on the position on the sky of the source through the geometric delay. The sinusoids created by changes in the geometric delay are called fringes, with a fringe phase ϕ defined by

$$\phi = \omega\tau_g. \quad (2.39)$$

In the case of an extended source, the response of the interferometer can be calculated by integrating over the sky brightness distribution I_ν :

$$R_c = \int I_\nu(\hat{s}) \cos(2\pi\nu\vec{b} \cdot \hat{s}/c) d\Omega. \quad (2.40)$$

Due to the cosine function in this response, it is only sensitive to the even part of the sky brightness distribution. To be able to detect the odd part of the sky brightness distribution, a sine is used instead of a cosine. This term is created by a second correlator in the interferometer, with a 90° phase delay to one of the antennas.

$$R_s = \int I_\nu(\hat{s}) \sin(2\pi\nu\vec{b} \cdot \hat{s}/c) d\Omega. \quad (2.41)$$

Together, these two responses create the *complex visibility*, defined as

$$V = R_c - iR_s = Ae^{-i\phi} \quad (2.42)$$

where the visibility amplitude A and the visibility phase ϕ are given by

$$A = \sqrt{R_s^2 + R_c^2}, \quad \phi = \tan^{-1}(R_s/R_c). \quad (2.43)$$

For an extended sky brightness distribution, we can then write the complex visibility as

$$V = \int I_\nu(\hat{s}) \exp(-i2\pi\vec{b} \cdot \hat{s}/\lambda) d\Omega. \quad (2.44)$$

From this equation something very important about interferometers becomes apparent. As we integrate over the target source, the direction unit vector \hat{s} changes. If this vector changes so much that we integrate over a complete fringe, we start to cancel out the signal. This means that a baseline is only properly sensitive to sources small enough that they fit within a fringe phase on the sky. That's why an interferometer needs both long and short baselines. The short baselines observe what the source looks like on large scales, and the long baselines observe what the source looks like on small scales.

In order to describe the baseline vector \vec{b} , a (u, v, w) coordinate system is used. In this coordinate system w is defined along the direction the interferometer is pointing in: \hat{s}_0 , and u and v point in the east- and north direction in a plane perpendicular to w . u , v and w can then be calculated as the components of \vec{b}/λ . In this coordinate system, l , m and n are used to describe the components of the unit direction vector \hat{s} . We can then calculate the complex visibility as

$$V(u, v, w) = \int \int \frac{I_\nu(l, m)}{\sqrt{1-l^2-m^2}} \exp[-i2\pi(ul + vm + wn)] dldm. \quad (2.45)$$

In the case that $w = 0$, this equation become a two-dimensional Fourier transform. Then the inverse Fourier transform can be taken to get the sky brightness distribution based on measurements in the u - v plane. Each baseline in an interferometer measures the complex visibility at one position in the u - v plane. For an interferometer with N antennas, it is possible to measure $N(N - 1)$ positions per frequency channel at any given time. The complete set of all positions in the u - v plane is called the *uv-coverage*. An example of uv -coverage can be seen in Figure 2.5. It is visible from the figure that as the Earth rotates around its axis, the uv -coverage changes. This allows us to measure the sky brightness distribution much better.

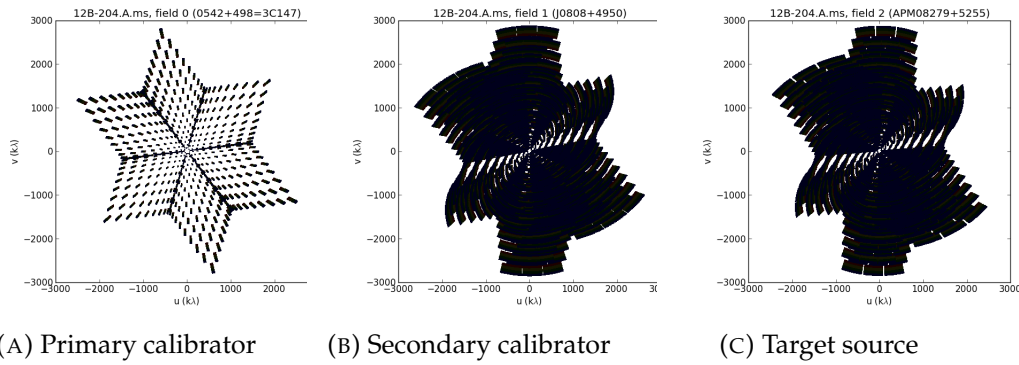


FIGURE 2.5: Plots of the uv-coverage for the two calibrators and the target source for one dataset.

2.4 Jansky Very Large Array

In this thesis we use data taken with the Jansky Very Large Array (JVLA). The JVLA is an interferometer located in New Mexico at an altitude of just over 2000 meters. It has 27 radio telescopes, each with a diameter of 25 meters, placed in a Y-shape. The JVLA has four baseline configurations: A through D, where the A-configuration is the configuration with the longest baselines, and the D-configuration has the shortest baselines. In A-configuration the JVLA has baselines between 0.68 km and 36.4 km, and in D-configuration the JVLA has baselines between 35 meters and 1.03 km. It is possible to observe all the way from 74 MHz to 45 GHz with the JVLA. In Figure 2.6 the position of the antennas in A-configuration is shown.

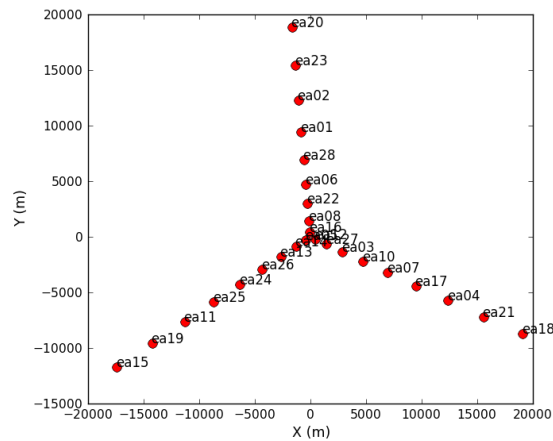


FIGURE 2.6: Antenna positions of the A-configuration of the JVLA.

Chapter 3

Data Reduction

3.1 Observations

From October to December in 2012, a total of 41 observations were made with the Jansky Very Large Array in A-configuration at a frequency of 23.844 GHz, with a bandwidth of 2 GHz. Two basebands were used with a bandwidth of 1 GHz each. Both basebands contain 8 spectral windows, and those spectral windows contain 64 spectral channels each. This gives a total of 1024 spectral channels with a channel width of 2 MHz or 26.2 km/s. Each of the 41 datasets were either an hour, an hour and a half, or three hours in duration. This gives a total of 79.5 hours of observing time. Taking calibration into account, this results in over 64 hours of on-target observing time; one of the deepest single object observations ever carried out with the JVLA.

In order to calibrate our measurements, each observation also includes measurements of either 3C147 or 3C286, and J0808+4950. As a primary calibrator, we shall use 3C147 or 3C286, and as a secondary calibrator we shall use J0808+4950.

Each dataset starts with a calibration of the pointing on the primary calibrator followed by an observation of the primary calibrator. Then the pointing on the secondary calibrator is calibrated. After that, there follows a sequence of observations where the secondary calibrator is observed for 60 seconds, and the target source is observed for 120 seconds.

3.2 Calibration

The data stored by the interferometer still has to be corrected before any meaningful results can be drawn from them. This is because the signal from the target source is altered by our atmosphere and the hardware in the interferometer. The visibilities that are stored in the raw data are called the *observed visibilities* V_{ij}^{obs} , where ij indicates the baseline between antennas i and j . During the calibration, we create calibration tables to turn these observed visibilities into *corrected visibilities*:

$$V_{ij}^{corrected} = G_{ij} V_{ij}^{obs} \quad (3.1)$$

where G_{ij} is the calibration table. These corrected visibilities can be used to get meaningful results. The calibration table G_{ij} can be the product of many different calibration tables:

$$G_{ij} = A_{ij} B_{ij} C_{ij} \dots \quad (3.2)$$

The calibration is performed using the CASA package developed by the NRAO. This software is specifically designed for processing data from single-dish radio telescopes and interferometers.

For calibration of the absolute flux density of the visibilities we use the primary calibrator, and for the calibration of the amplitudes and phases of the visibilities as a function of time we use the secondary calibrator.

The calibration starts by retrieving calibration tables for the antenna positions, gain elevation curves, and atmospheric opacity from the NRAO. During each array cycle the position of each antenna is measured, but there can be deviations on the order of a couple millimeters. These deviations are measured during the observation. Since the baselines in the interferometer are very important, it is essential to know the positions of the antennas accurately. The gain elevation curves correct for any changes in the gain due to deformations of the antenna. This is important for the amplitudes of the visibilities. Finally, the atmospheric opacity tables correct for attenuation of the signal based on the weather conditions at the time of the observation. The opacity is needed for the absolute flux density calibration. This is important for this thesis since the observing frequency is close to the atmospheric water vapor line at 22 GHz. An example of the weather conditions during an observation can be found in Figure 3.1.

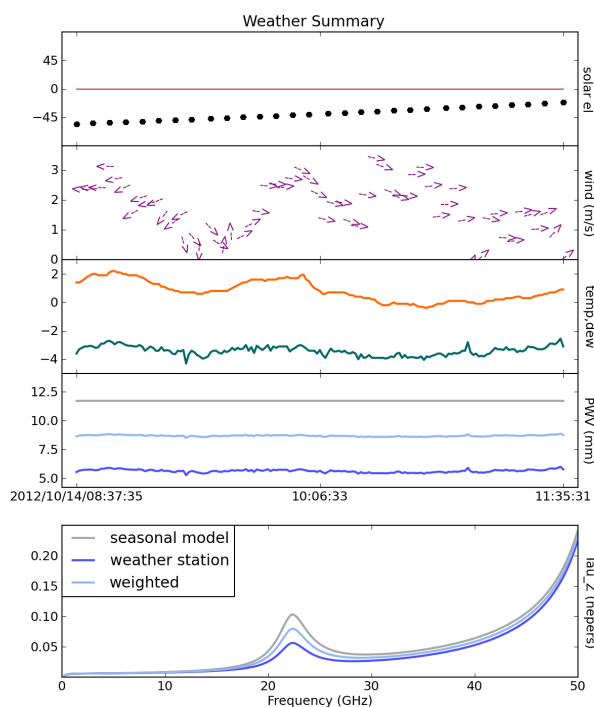


FIGURE 3.1: Weather conditions during one of the observations. In the top plot, the solar elevation is shown. The next plot shows the wind speed and direction. Then a plot of the temperature and dew point follows. After that comes a plot of the total amount of precipitable water vapor in the atmosphere. The final plot shows the opacity at zenith as a function of frequency. The peak at 22 GHz comes from absorption due to water vapour in the atmosphere.

After retrieving those tables, we go through the data to look for errors in the visibilities. Most of the errors are caused by starting the observation before all antennas are on-source or by a defective receiver in one of the antennas. Once these errors are found, they are flagged to make sure they are not used for calibration or imaging. See Figure 3.2 for an example of this for a primary calibrator. See Figure 3.3 for an example of flagging bad data for a secondary calibrator.

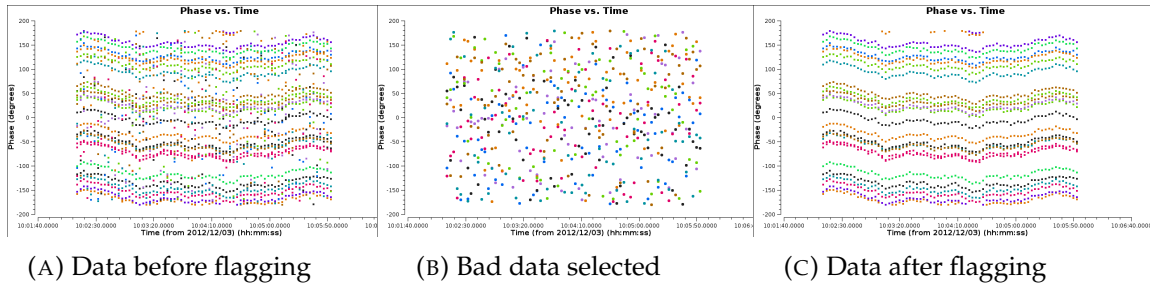


FIGURE 3.2: Plots of the phase versus time of a baseline for the primary calibrator. The colorization indicates the spectral windows. In Figure A, there is a clear case of bad data throughout the observation. In Figure B, this bad data is selected. In this particular case, it was a defective receiver in one of the basebands. In Figure C, this bad data is flagged out, and all reliable data remains.

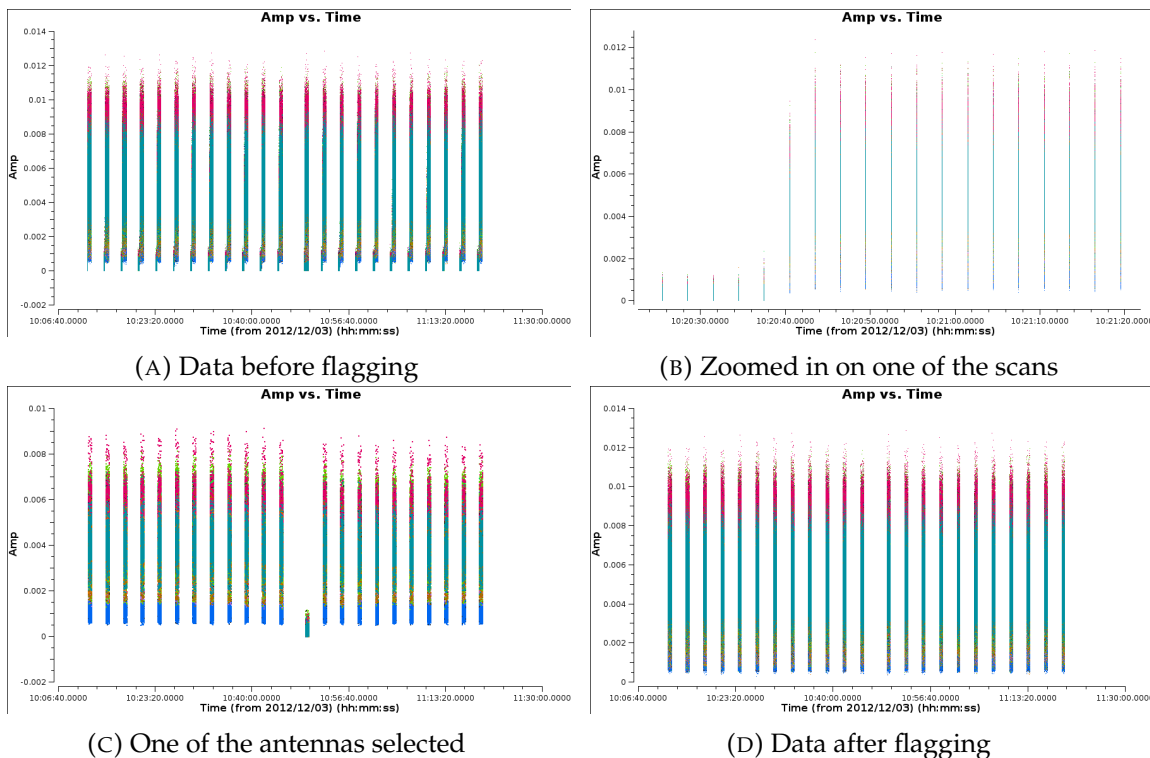


FIGURE 3.3: Plots of the amplitude versus time colorized by spectral window of the secondary calibrator. In Figure A the raw data is shown. Figure B is a zoomed-in plot of one of the scans from Figure A. On the left of Figure B, there is bad data visible. Such data is flagged out. In Figure C a plot is shown of all data related to a single antenna. It is clearly visible that one scan failed for this antenna. This data is also flagged. Figure D shows the plot of the final data.

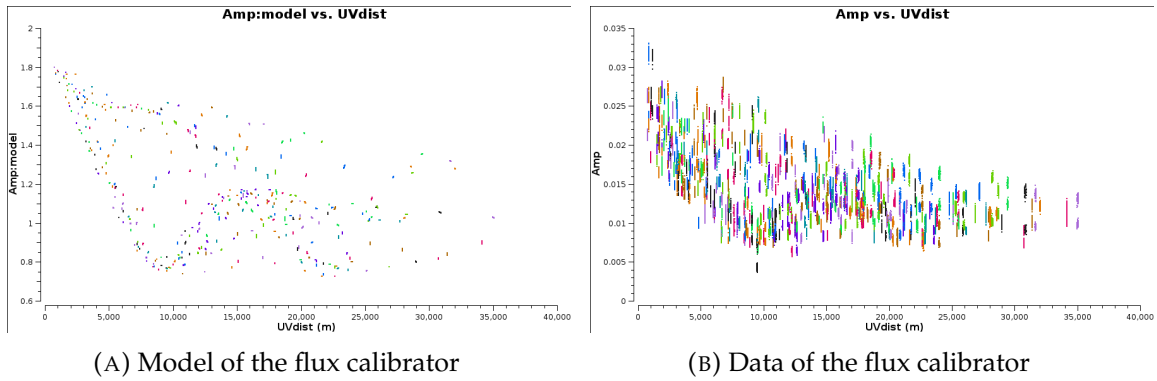


FIGURE 3.4: Plots of the amplitude versus baseline length of the flux calibrator for one spectral window. The colorization indicates the different baselines.

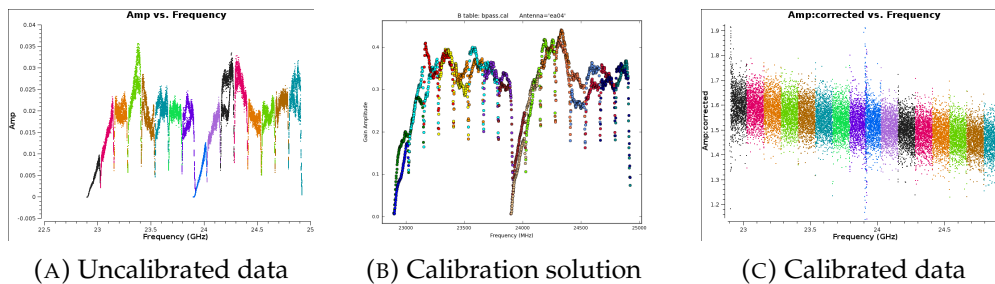


FIGURE 3.5: Amplitude versus frequency plots of the flux calibrator for a single baseline. The colours indicate the different spectral windows. In Figure A the flagged data is shown before the bandpass calibrations are applied. Figure B shows the calibration solutions based on the uncalibrated data and the model of the flux calibrator. Finally, Figure C shows the calibrated data.

In order to calibrate the flux density of the target, we compare our measurements of a known source - our primary calibrator - with what we think this source should look like if we observed it with our interferometer. To do that, we first use the task *setjy* in CASA to generate a table of visibilities based on a model of the flux calibrator and our u-v positions. An example of this is shown in Figure 3.4.

Once this model is generated, we use the CASA task *gaincal* to create a rough phase calibration table for the primary calibrator as a function of time relative to one antenna based on a small part of each spectral window. Since these errors tend to be the dominant effect, it is important to have a solution for them before proceeding with the rest of the calibration. We do not use this calibration solution for our target though. For our target we use a phase calibration solution based on the secondary calibrator. Since we know that the secondary calibrator is a point-source, we expect the phases to be $\phi = 0$ for all baselines. This allows for a more reliable calibration solution.

Using the calibration for the phases as a function of time, we use the CASA task *gaincal* again to solve for antenna-based residual delays as a function of frequency for the primary calibrator. These delays originate from the electronics in each receiver, and are on the order of a couple nanoseconds.

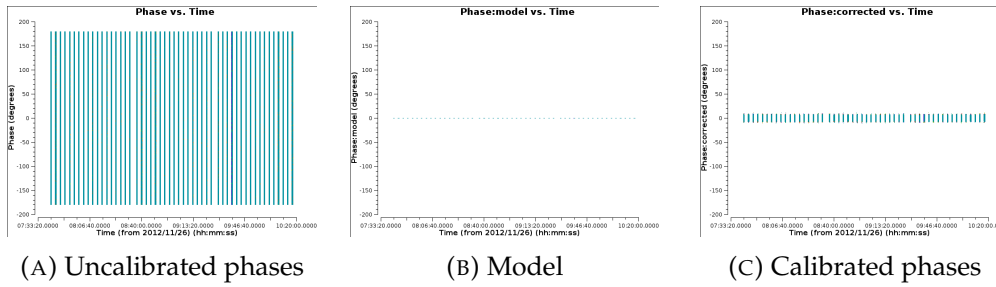


FIGURE 3.6: Phase versus time plots of the secondary calibrator. Figure A shows the phases before calibration. Figure B shows the model of what the phases should be (all 0). Finally, Figure C shows the calibrated phases versus time.

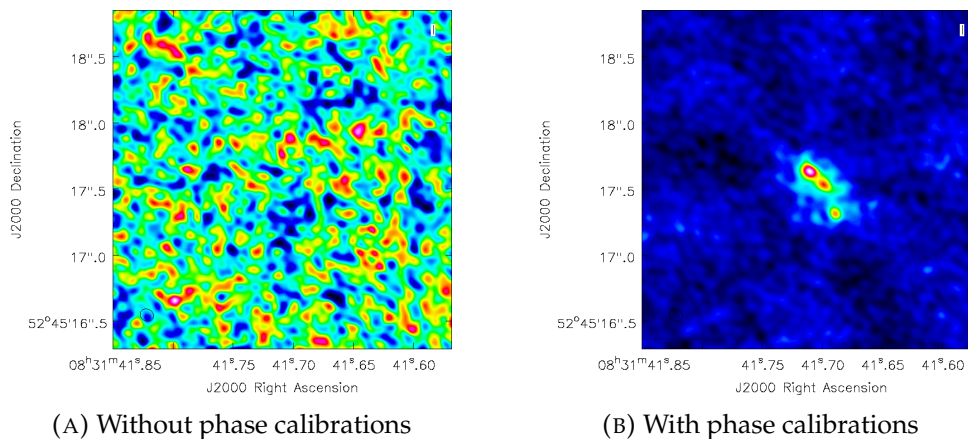


FIGURE 3.7: Images of the target source before and after applying phase calibrations.

After the calibration table for the residual delays has been created, we proceed with calibrating the bandpass. This has to be done because the receiver is not equally sensitive to all frequencies. By comparing measurements of the amplitude as a function of frequency for the primary calibrator with the model of what the spectrum of the primary calibrator should be like, this calibration table can be constructed. The CASA task *bandpass* is used for this. The result of this can be seen in Figure 3.5.

Now that the delay calibrations and the bandpass calibrations are known, we can calculate the phase calibrations properly. This is done for both the primary and the secondary calibrator. See Figure 3.6 for plots of the phases before and after calibration. The effect of the phase calibrations is shown in Figure 3.7.

Using the flux calibration solution for the primary calibrator, we can determine a calibration solution for the flux density of the secondary calibrator by using the CASA task *fluxscale*. After that, we can also determine calibration solutions for the initial phases, delays, and bandpass of the secondary calibrator like we did before with the primary calibrator. Next, we can apply the primary calibration solutions to the primary calibrator and the secondary calibration solutions to the secondary calibrator by simply multiplying the amplitude and phase calibration solutions onto the observed visibilities. For the target source, we use the calibration solutions of the secondary calibrator. However, the phase solutions are a bit more complicated, since they will have to be interpolated in time. After applying all the calibration solutions to the calibrators and target field, we get a set of true visibilities.

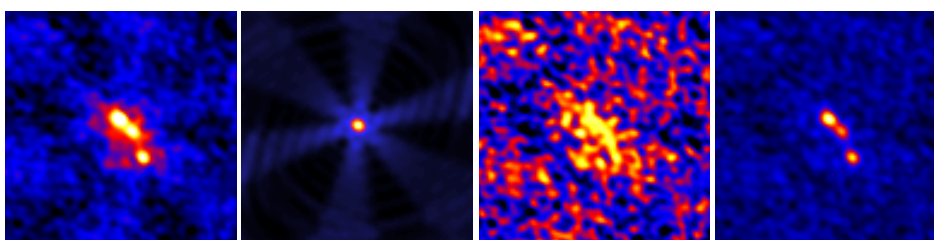
3.3 Imaging

Since all our data is located in the u - v plane, we have to do a Fourier transform on it to get an actual image of our target source. However, since we can never have a complete uv -coverage, this image contains artifacts. Therefore, we call this image the *dirty image*. We can say that the dirty image is a convolution of the actual sky brightness distribution with the so-called *dirty beam*. The dirty beam describes the point spread function of the interferometer. This is simply the Fourier transform of the uv -coverage.

Under the assumption that we can represent our sky brightness distribution by a small number of point sources, we can use the CLEAN algorithm as introduced by Högbom (1974) to improve the quality of the image. The idea behind the CLEAN algorithm is that it is possible to get the true sky brightness distribution by deconvolving the dirty image and the dirty beam.

First, the dirty beam is constructed from the uv -coverage. Next, a region in the image is selected where the target source is thought to be. In this region, the brightest spot is located, and a delta function convolved with the dirty beam is subtracted. This delta function is then stored in a file containing the model of the target source. This process of finding the brightest spot, subtracting flux from there, and storing the delta function in a model is repeated multiple times until some threshold is reached. The threshold is generally taken to be higher than the noise level in the image. Once the threshold is reached, the set of delta functions taken from the dirty image is convolved with a *clean beam*, which generally is an elliptical Gaussian. After that, the residuals from the dirty image are added to create a *clean image*.

What this accomplishes is that the side-lobe structure in the image as caused by the dirty beam is removed from the image. Since the residuals are added again, we keep all information about noise levels, and we do not have to worry about missing flux in our clean image of the target source.



(A) Image before CLEANing (B) Dirty beam (brightened) (C) Residuals from CLEANing (D) CLEANed image

FIGURE 3.8: Images of the CLEANing process. Figure A shows the target source before CLEANing. Figure B shows an edited image of the dirty beam to show the structure more clearly. Figure C shows the residuals from the CLEANing process after the threshold has been reached. It clearly shows that the CLEANing stopped before the noise level was reached. Finally, Figure D shows the final image.

Chapter 4

Results

4.1 Dataset summary

After finding the calibration solutions for each of the 41 datasets, we apply these calibration solutions to get 41 calibrated datasets. These datasets were CLEANed using natural weighting, and the flux density of the quasar, and the rms noise in the image was measured for each of them. A summary of this can be found in Table 4.1.

4.2 Continuum emission

In order to improve the noise levels in the image, we concatenated all the datasets together to get one dataset containing all the calibrated data. This dataset was CLEANed, while excluding the spectral channels of the CO emission, to create an image of the continuum emission from the host quasar with a resolution of $0.11'' \times 0.09''$ and an rms noise of $1.4 \mu\text{Jy beam}^{-1}$. This image is shown in Figure 4.1. The three gravitationally lensed images can be clearly distinguished, and at first sight the emission appears to be unresolved.

To check if the emission from the quasar is indeed unresolved, we tried to fit two-dimensional Gaussians to each of the three images of the quasar using the CASA task *imfit*. If the emission is unresolved, a two-dimensional Gaussian would result in a good fit for the data. The result of this fitting is shown in Figure 4.2. As can be seen from the residuals, the two-dimensional Gaussians do not result in a good fit for the data. The residuals show extended emission surrounding the quasar up to $0.3''$ away from the center of the peaks, but also a strong compact and unresolved component. The possibility that the extended emission is an artifact caused by improper CLEANing is excluded, since the brightness of this extended structure exceeds the threshold used during the CLEANing.

#	Start	On-source time (s)	Flux density (μJy)	rms noise ($\mu\text{Jy beam}^{-1}$)	Beam size (arcsec)	Pos. angle (deg)
1	2012 - Oct - 6, 15:37	3975	464	10.8	0.105 x 0.089	-33.4
2	2012 - Oct - 11, 12:18	3978	340	10.1	0.107 x 0.086	48.9
3	2012 - Oct - 13, 13:10	3978	414	9.9	0.106 x 0.088	14.1
4	2012 - Oct - 14, 8:37	9273	402	7.2	0.135 x 0.086	82.5
5	2012 - Oct - 15, 8:33	9273	399	6.4	0.137 x 0.088	88.5
6	2012 - Oct - 15, 11:33	3975	388	9.8	0.120 x 0.090	38.8
7	2012 - Oct - 16, 8:29	9270	391	5.8	0.129 x 0.091	80.5
8	2012 - Oct - 16, 11:29	9273	377	5.3	0.098 x 0.087	24.0
9	2012 - Oct - 17, 8:55	9273	360	7.5	0.115 x 0.087	80.0
10	2012 - Oct - 23, 8:41	3978	432	10.4	0.134 x 0.090	81.1
11	2012 - Oct - 23, 11:57	3975	399	10.1	0.111 x 0.086	11.1
12	2012 - Oct - 24, 8:52	3975	397	12.6	0.143 x 0.089	81.3
13	2012 - Oct - 29, 11:37	3978	403	8.3	0.098 x 0.086	27.1
14	2012 - Nov - 2, 8:52	3975	455	8.3	0.113 x 0.091	74.8
15	2012 - Nov - 5, 7:56	3975	398	8.9	0.126 x 0.095	78.3
16	2012 - Nov - 6, 7:11	3975	416	10.0	0.141 x 0.089	-86.9
17	2012 - Nov - 13, 6:41	7119	405	7.0	0.138 x 0.090	-87.7
18	2012 - Nov - 14, 6:35	9273	468	5.9	0.125 x 0.089	87.5
19	2012 - Nov - 16, 8:02	3975	359	11.5	0.130 x 0.091	62.8
20	2012 - Nov - 17, 6:23	3975	394	9.6	0.147 x 0.091	89.7
21	2012 - Nov - 21, 12:06	9273	409	8.4	0.103 x 0.087	13.0
22	2012 - Nov - 24, 14:24	3975	390	8.0	0.123 x 0.087	-84.6
23	2012 - Nov - 25, 6:22	9273	422	5.8	0.116 x 0.090	78.3
24	2012 - Nov - 25, 9:21	9273	425	5.3	0.096 x 0.086	10.3
25	2012 - Nov - 26, 7:18	9270	442	4.9	0.105 x 0.090	61.0
26	2012 - Nov - 29, 14:05	3978	392	8.8	0.126 x 0.089	-74.9
27	2012 - Dec - 2, 5:54	3978	443	8.0	0.133 x 0.088	88.1
28	2012 - Dec - 3, 9:50	3975	386	8.4	0.104 x 0.086	-175.6

#	Start	On-source time (s)	Flux density (μJy)	rms noise ($\mu\text{Jy beam}^{-1}$)	Beam size (arcsec)	Pos. angle (deg)
29	2012 - Dec - 5, 5:57	3975	410	9.0	0.123 x 0.088	83.7
30	2012 - Dec - 5, 7:57	3978	393	8.1	0.101 x 0.088	43.4
31	2012 - Dec - 6, 5:24	3975	388	7.9	0.141 x 0.091	86.0
32	2012 - Dec - 6, 13:37	3975	422	8.5	0.129 x 0.088	-85.8
33	2012 - Dec - 7, 5:20	3978	345	10.2	0.140 x 0.091	82.6
34	2012 - Dec - 7, 13:33	3978	340	8.5	0.128 x 0.088	-77.4
35	2012 - Dec - 8, 13:59	3975	389	9.7	0.134 x 0.089	-88.4
36	2012 - Dec - 10, 6:52	9273	408	5.3	0.104 x 0.088	57.2
37	2012 - Dec - 10, 12:52	3978	423	7.4	0.115 x 0.091	-78.5
38	2012 - Dec - 17, 4:26	9270	433	6.7	0.120 x 0.087	86.3
39	2012 - Dec - 21, 5:10	9270	458	6.1	0.116 x 0.087	72.1
40	2012 - Dec - 22, 7:37	3972	475	9.5	0.104 x 0.086	36.0
41	2012 - Dec - 29, 9:37	2088	440	11.2	0.099 x 0.091	-174.9

TABLE 4.1: Summary of all datasets. The flux density was measured by integrating the flux over a constant region on the sky with a size of 15.4 beam sizes. The rms noise was measured in a region on the sky without any emission from the quasar.

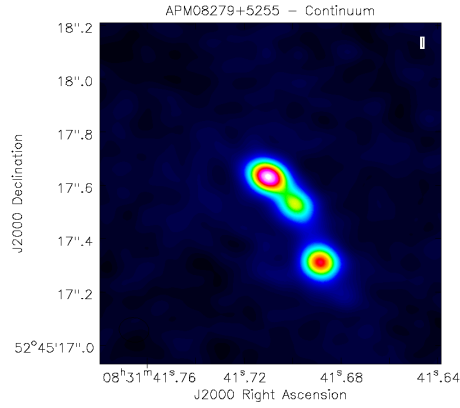


FIGURE 4.1: CLEANed continuum image of APM08279+5255

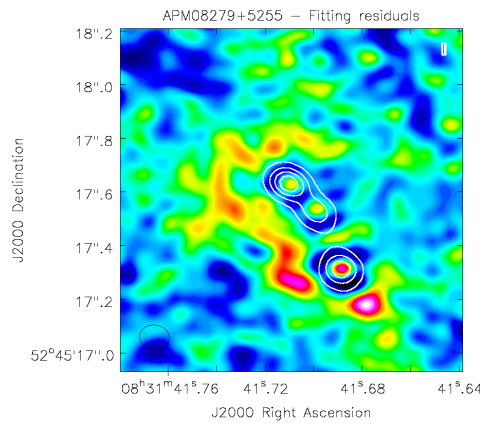


FIGURE 4.2: Residuals of fitting two-dimensional elliptical Gaussians to the continuum image. The contours indicate the continuum emission.

Instead of measuring the flux density by fitting Gaussians, we measured the total flux density of the image by integrating over the flux within a region on the sky within which we believe the source to be. For the uncertainty in the total flux density, we use the rms noise, and an estimation of the uncertainty due to calibration errors. The total uncertainty is then calculated as following:

$$\sigma_{total} = \sqrt{\sigma_{rms}^2 * N_{beam} + \sigma_c^2} \quad (4.1)$$

where σ_{rms} is the rms noise, N_{beam} is the amount of beam sizes in the region on the sky over which the flux was integrated, and σ_c is the uncertainty in the calibration, which we will take to be 5% of the total flux density as recommended by Perley et al. (2017). This results in a final estimate of the flux density of $406 \pm 22 \mu\text{Jy}$.

Instead of measuring the total flux density of the three images together, we can also measure the brightness ratios of the images. For image A, we find a brightness of $113.9 \pm 1.4 \mu\text{Jy beam}^{-1}$, for image B, we find a brightness of $87.3 \pm 1.4 \mu\text{Jy beam}^{-1}$, and for image C we find a brightness of $63.9 \pm 1.4 \mu\text{Jy beam}^{-1}$. The uncertainties are taken as just the rms noise, since calibration errors will be divided out for the brightness ratios. Using these peak brightnesses we find brightness ratios of $b(A, B) = 0.766 \pm 0.015$ and $b(A, C) = 0.561 \pm 0.014$, where the uncertainty follows from propagation of uncertainty.

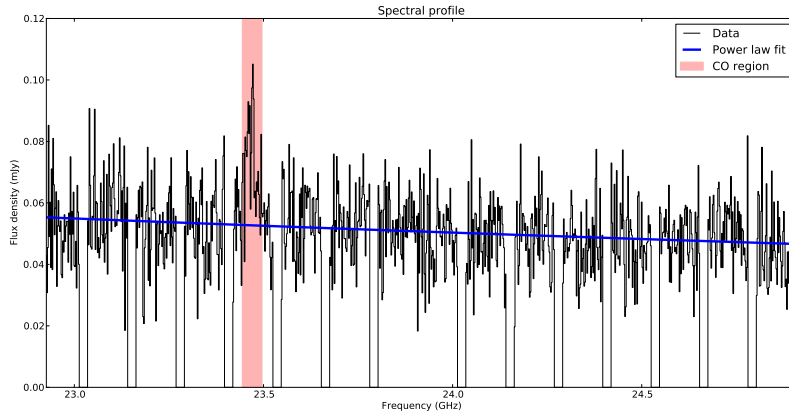


FIGURE 4.3: Spectrum of the emission from APM08279+5255. The blue line indicates the power law fit with a spectral index of -2.0, and the red region indicates the spectral windows that were excluded from the fitting due to the CO line.

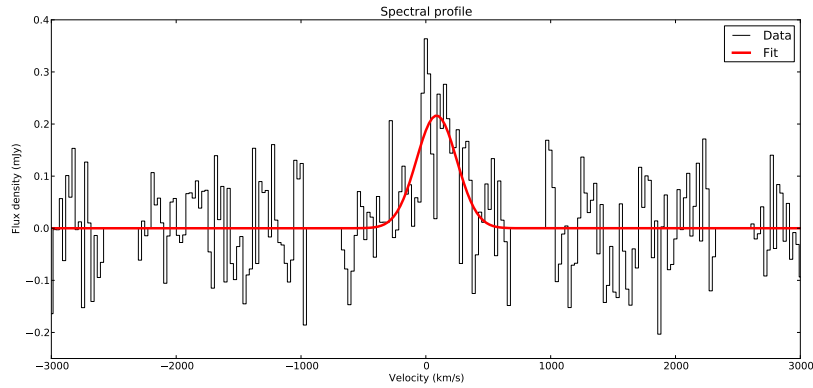


FIGURE 4.4: Spectrum of the CO-line in APM08279+5255. The red line indicates the least-squares Gaussian fit.

In addition to making an image of the continuum emission, we can plot the continuum spectrum and fit a line through it to find a slope. We fitted a power law of the form $S_\nu \propto \nu^\alpha$ through the data, while excluding the spectral channels of the CO line and the edges of the spectral windows. The result is shown in Figure 4.3. There is a clear slope visible in the spectrum of APM08279+5255. From the fitting procedure we derive a spectral index of $\alpha = -2.0 \pm 0.3$, where the uncertainty follows from the covariance matrix.

4.3 CO($J = 1 \rightarrow 0$)

In order to make a spectrum of the CO line, we first use the CASA task *uvcontsub* to make a model of the continuum spectrum, and subtract that from the total spectrum. That results in a dataset containing only noise and the CO emission. We can now make an image of the quasar while keeping the spectral information. The resulting image has channels of 26.2 km/s, and an rms noise of $31 \mu\text{Jy beam}^{-1} \text{ channel}^{-1}$.

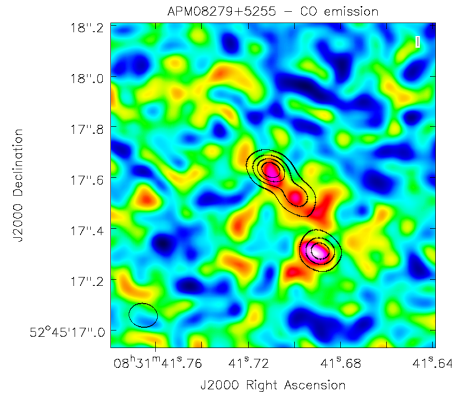


FIGURE 4.5: Image of the CO emission from APM08279+5255. The contours indicate the position of the continuum emission

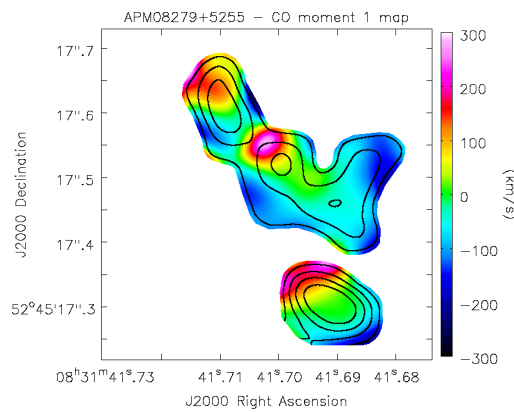


FIGURE 4.6: Moment-1 map of the CO emission in APM08279+5255. The contours indicate the position of the CO emission.

There are other sources of uncertainty present (such as the calibration errors), but these are negligible compared to the rms noise per channel.

A plot of the spectrum of the continuum-subtracted data at the location of the quasar is shown in Figure 4.4. By fitting a Gaussian through the spectral data, we derive an amplitude of 0.216 ± 0.028 mJy, and a full-width at half-maximum of 380 ± 57 km/s. The uncertainties follow from the covariance matrix. This gives an integrated flux of 87 ± 17 μ Jy km/s. The signal-to-noise ratio is calculated by taking the peak brightness of the CO line and dividing that by the rms noise within the FWHM. For the rms noise we take the rms noise per channel and divide that by the square root of the amount of channels in the FWHM. This gives a signal-to-noise ratio of 26.

In addition to plotting the spectrum of the CO($J = 1 \rightarrow 0$) line, we made an image of the CO emission. This is done by CLEANing the continuum-subtracted dataset. To reduce noise, we only selected the spectral channels where the CO line is found. This results in the image shown in Figure 4.5. From this image, it is clear that the CO emission generally traces the continuum emission, apart from a structure to the west of the quasar. This structure appears to also have been observed by Riechers et al. (2009). Also, the CO emission appears to be the brightest in the southern image.

Apart from imaging the position of the CO emission, we can make a moment-1 map to show the line-of-sight velocity of the CO emission. This map is shown in Figure

4.6. It is visible in the moment-1 map that the CO gas appears to have a higher line-of-sight velocity to the northeast of each individual image, while the line-of-sight velocity appears lower in the southwest.

4.4 Time variations

Since the 41 observations that we have span a time range of almost three months, we checked if there is any time variability visible in the flux density. Time variations on such short scales would indicate that (part of) the emission comes from a compact source, which would most likely be the AGN.

Based on earlier results, we decided to measure the flux density not by fitting Gaussians, but rather by measuring the total flux density within a region on the sky. This region is based on the continuum image of the complete dataset, and is constant for all measurements. A plot of the flux density as a function of time is shown in Figure 4.7.

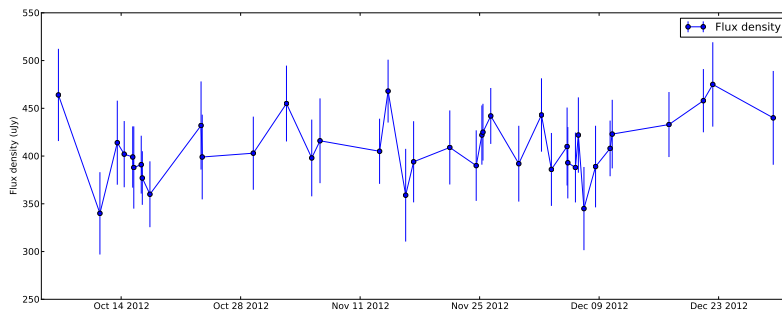


FIGURE 4.7: Plot of the time variations in the total flux density as a function of time. The uncertainties are based on the rms noise in the individual images and an estimate of the error due to calibration, as before.

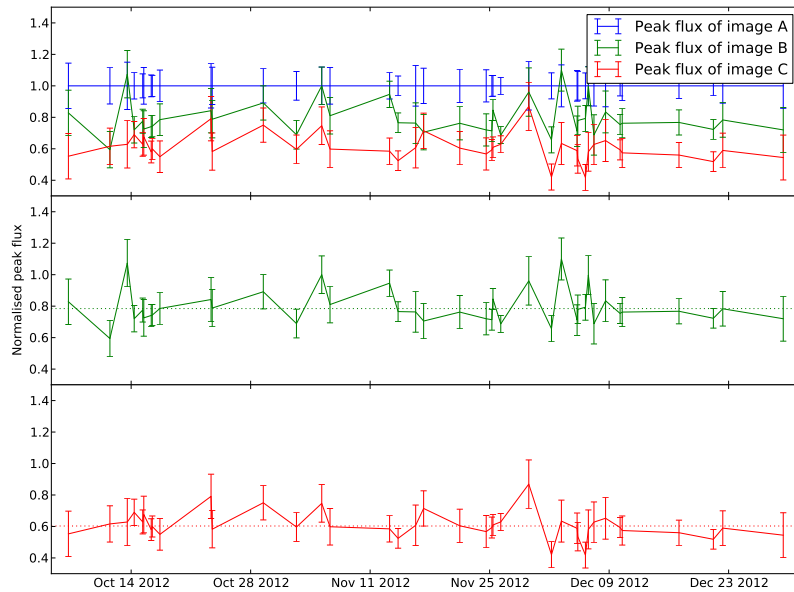


FIGURE 4.8: Plot of the normalized peak fluxes with respect to image A of each of the images as a function of time. The uncertainties are based on the rms noise in the image. The top image shows all three images together, and the bottom two plots show the normalised peak flux of image B and C. The dotted line represents the average peak flux.

Based on the uncertainties, there is no convincing evidence that there are time variations in the total flux density. As a second check we measured the peak flux of each of the images in each dataset, and plotted that against time. The resulting plot is shown in Figure 4.8.

This time there are variations visible. If there would be no time variations, the normalised peak fluxes would remain constant. Also, amplitude calibration errors are normalized out, leaving only the uncertainty due to rms noise. There are 4 data points visible where the peak flux of image B approaches or even exceeds the peak flux of image A. Three of these peaks show $2\text{-}\sigma$ deviation in the peak flux of image B from its mean. In the first and fourth peak, the normalized peak flux of image C shows no deviation, so it is most likely image B that is deviating from its mean. In the second and third peak, the normalized peak fluxes of image B and image C both approach image A, so it will most likely be image A that is deviating. In addition to the strong deviations, it appears like there is some correlation between some datapoints. Around the 14th of December, there are 6 datapoints where the normalised peak fluxes seem to follow a pattern. Also, in the last 7 datapoints the normalised peak fluxes of image B and image C appear to be strongly correlated.

4.5 Wide-field imaging

To check if there were any other sources detected along with APM08279+5255, an image was made with the scale of the primary beam of one of the antennas in the interferometer: $\sim 1.8'$. In order to increase the sensitivity, we applied a taper of $0.2''$. In Figure 4.9, the wide-field image is shown. There appears to be one source $\sim 3''$ south of APM08279+5255. Fitting a two-dimensional Gaussian to this source results in a total flux density for this source of $39.6 \pm 3.6 \mu\text{Jy}$, where the uncertainty is based on the covariance matrix and a 5% calibration error. Since there appears to be no structure left from the source in the residuals, we find this fit to be reliable. Apart from this one source, there is no other object visible in the image.

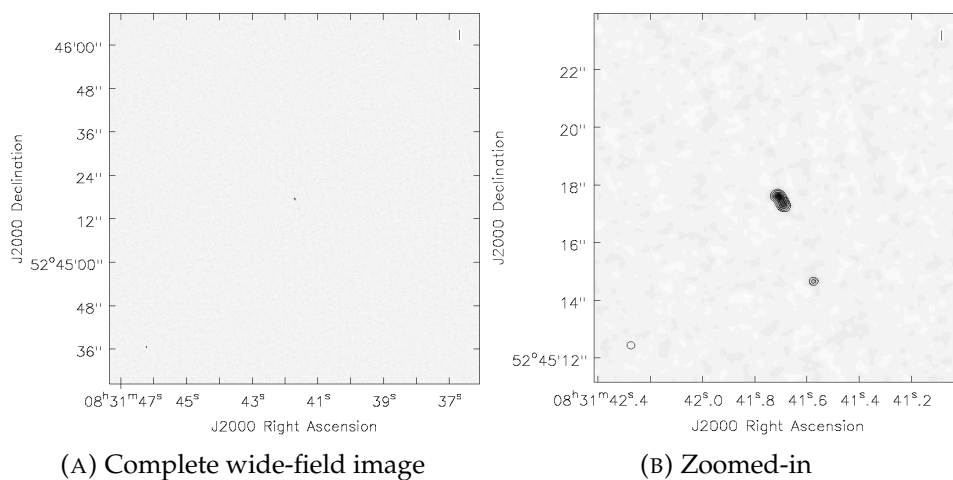


FIGURE 4.9: Wide-field image of the environment of APM08279+5255. The contours indicate the relative levels of 0.1, 0.2, 0.4, 0.6 and 0.8.

Chapter 5

Discussion

In this thesis we have presented new high-resolution radio images of the gravitationally lensed quasar APM08279+5255, obtained with the JVLA. This data was analysed to determine the cause of the continuum emission at an observed frequency of 23.9 GHz, and to find if the CO($J = 1 \rightarrow 0$) can be resolved. A number of results follow from this analysis.

5.1 Continuum imaging

From the continuum image we find that there is a strong unresolved component at a scale of $0.1''$, as well as a weak extended component. By integrating the flux over a region on the sky, we derive a total flux density of $406.4 \pm 22 \mu\text{Jy}$. Additionally, we derive that the continuum emission has a spectral index of -2.0 ± 0.3 .

In order to get an idea about what our measurement of the total flux density means, we compare it to measurements of the flux density of APM08279+5255 at different frequencies. Stacey et al. (2017) fitted two greybody spectra and one power-law through measurements ranging from 1.4 GHz to 5 THz. In Figure 5.1, the fit for the spectral energy distribution of APM08279+5255 is shown. According to the fit, the flux density at 23.9 GHz should be $246.0 \mu\text{Jy}$. However, we have measured $406.4 \pm 22 \mu\text{Jy}$. This means that we have an excess in flux density of approximately $160 \mu\text{Jy}$. It is important to note that the fit only included two greybodies and one synchrotron spectrum. It is very possible that there is a free-free component in the spectrum of APM08279+5255. That could explain the excess of flux density that we measure.

The slope that we measure wouldn't be explained by a free-free component though. A synchrotron self-absorption component is unlikely, because it would have to turn over very rapidly in order to match the rest of the data points. Also, steepening of the synchrotron component due to higher energy electrons radiating their energy away first is unlikely because our measurement lies above the fit, not below. A final option is that the emission from the quasar is variable in time. Since other measurements of the flux density are taken at different times, it may be the case that the spectral energy distribution at that time was different as well.

We can also compare our brightness ratios to the brightness ratios as predicted by the model for the gravitational lens by Riechers et al. (2009). The model for the gravitational lens by Riechers et al. predicts brightness ratios of $b(A, B) = 0.84$ and $b(A, C) = 0.57$, while we found $b(A, B) = 0.766 \pm 0.015$ and $b(A, C) = 0.561 \pm 0.014$. The brightness ratios $b(A, C)$ agree with each other within the uncertainties, while $b(A, B)$ does not agree within the uncertainties. A possible explanation for this could be that the proposed lens model needs adjustment, but it could also point towards time variability of the source.

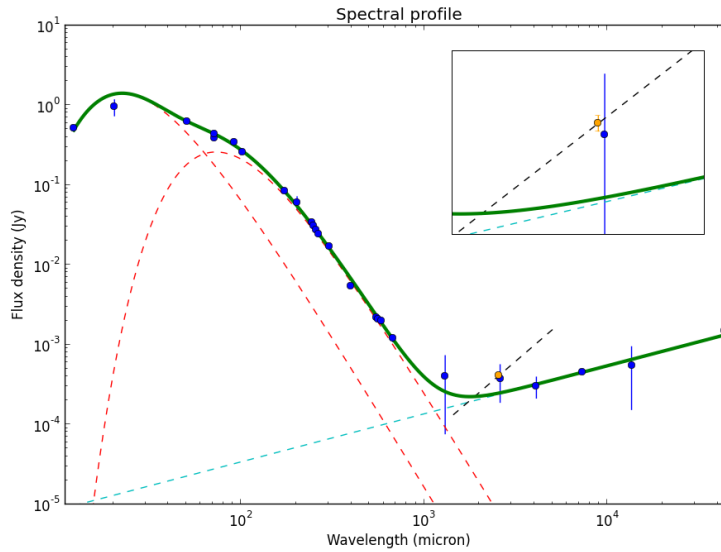


FIGURE 5.1: Spectral energy distribution of APM08279+5255. The blue data points indicate the data points as given by Stacey et al. (2017), and the orange data point indicates the flux density as derived in this thesis. The green line represents the fit by Stacey et al. (2017) and the red and cyan dashed lines represent the components of the fit. The two greybodies have a temperature of 41K and 135K, both with a dust-emissivity index of $\beta = 1.8$, and the power law has a slope of -0.6 . The black dashed line represents the slope of the continuum as fitted in Chapter 4.2. In the top-right corner a zoomed-in view of the new datapoint is shown.

5.2 CO($J = 1 \rightarrow 0$)

By subtracting the continuum emission from the data, we were able to make a map of the CO emission. Additionally, the spectrum of the CO line was plotted and a Gaussian was fitted to determine the properties of the CO line. Finally, an attempt was made to make a moment-1 map of the CO emission.

The CO emission is clearly detected, but remains unresolved in the individual peaks. There is a detection of CO emission to the west of the quasar, even though the continuum image does not show emission there. Also, the flux ratios of the individual peaks do not correspond to the flux ratios in the continuum image. Apart from the structure to the west of the quasar, the emission does not seem to be extended, so this would suggest that most of the CO emission comes from a region close to the AGN. Since the structure to the west of the quasar also appears to have been observed by Riechers et al. (2009), we believe that this structure is real.

Riechers et al. (2009) derive a peak brightness of the CO emission of $210 \pm 19 \mu\text{Jy beam}^{-1}$, compared to our $216 \pm 28 \mu\text{Jy beam}^{-1}$. These values agree very well. However, in an earlier paper (Riechers et al., 2006) they derive a FWHM of $556 \pm 55 \text{ km/s}$ using GBT data, compared to our FWHM of $380 \pm 57 \text{ km/s}$. This difference in FWHM also causes a difference in integrated flux: $168 \pm 15 \mu\text{Jy km/s}$ versus our $87 \pm 17 \mu\text{Jy km/s}$. The reason why the peak brightness values agree, but the FWHM do not is unknown.

Finally, the moment-1 map of the CO emission shows that the CO emission around the three images has a higher radial velocity towards the northeast, and a lower radial velocity towards the southwest. The fact that all three images show similar behaviour would suggest that this apparent motion is real. However, image A and image C are too close together to properly resolve motion of the gas, and the structure to the west may also influence the image. Therefore, we remain cautious while interpreting this map.

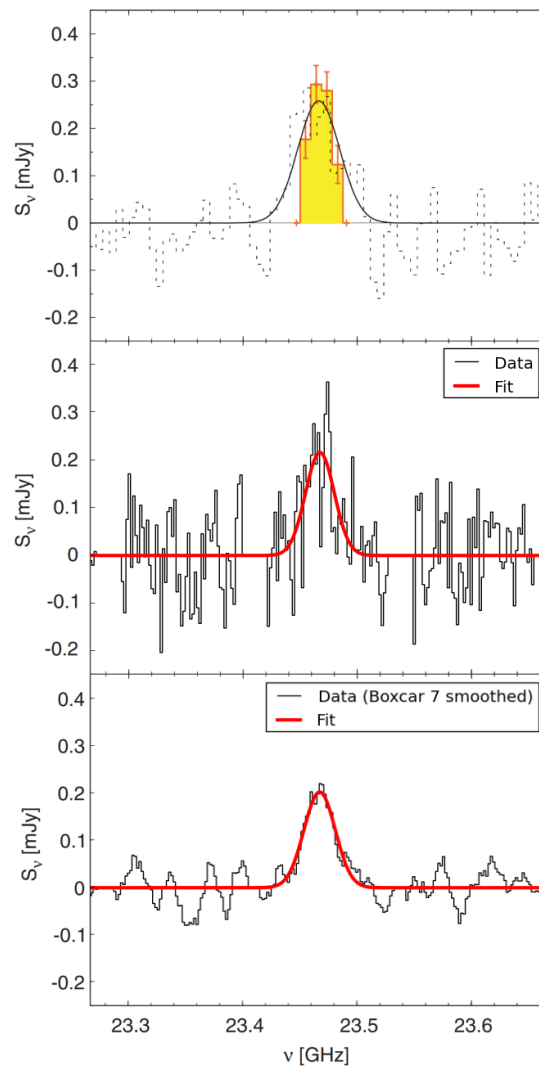


FIGURE 5.2: Comparison of the CO line spectrum. The top plot shows the spectrum of the CO line as found by Riechers et al. (2009) and Riechers et al. (2006). The dashed line indicates the GBT spectrum, and the yellow data represents the VLA data. The middle plot shows the spectrum of the CO line as found by us, and the bottom plot shows a smoothed spectrum (boxcar 7) of the CO line as found by us.

5.3 Time variations

In order to find evidence for time variability in the continuum emission of APM08279+5255, we have measured the total flux density and the normalized peak fluxes of the individual images, and plotted that as a function of time.

The time variations in the total flux density of the quasar do not significantly exceed the uncertainties. This may be caused by our area of integration being too large, which introduces a lot of rms noise. Small fluctuations in the flux density will then be hidden by that noise.

The time variations in the the normalized peak brightnesses of the individual images do show large deviations from their average normalized peak brightnesses on the order of $2\text{-}\sigma$. Further inspection of these datasets (3, 15, 28 & 32) shows no odd features like significant phase errors or highly-elliptical beams. Therefore, it seems like these deviations may be real. Since these deviations occur on a timescale of days, it must come from a very compact source like the AGN. There is not yet enough evidence to conclude that there are actual time variations, but the data that we have certainly warrants further research on this topic.

5.4 Wide-field imaging

Our wide-field image does not show any other sources nearby APM08279+5255, apart from one unknown radio source approximately $3''$ south of our quasar. This object has been detected previously by Riechers et al. (2009), although they explicitly state that they could not detect the radio source at a frequency of 23.5 GHz. This may be explained by their rms noise level of $19 \mu\text{Jy beam}^{-1}$, which is quite large compared to the flux density of $39.6 \pm 3.6 \mu\text{Jy}$ that we find. They were able to detect it at 4.5 GHz and 8.4 GHz, where they find flux densities of $180 \pm 40 \mu\text{Jy}$ and $83 \pm 10 \mu\text{Jy}$ respectively. Adding our data point to that, we find the spectral energy distribution as shown in Figure 5.3. From the fit, we derive a spectral index of -0.8 ± 0.1 .

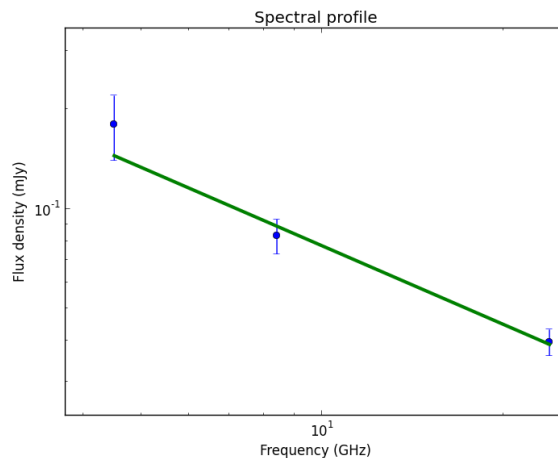


FIGURE 5.3: Spectral energy distribution of the radio source $3''$ south of APM08279+5255. The data points at 4.5 GHz and 8.4 GHz are given by Riechers et al. (2009). The green line represents the least-squares fit of a power law through the data points.

5.5 Identifying the cause of radio emission

One of the main goals of this thesis is to determine whether the continuum emission of APM08279+5255 at an observed frequency of 24 GHz is due to star-formation or AGN-related activity. There are several things that we can look at for this. First of all, previous research shows that APM08279+5255 lies right on the radio-FIR correlation (Riechers et al., 2009). This suggests that the synchrotron and FIR emission is due to star-formation activity, but they find that the Condon model does not give a reasonable fit for the spectral energy distribution. The Condon model was expected to give a good fit, since the Condon model assumes that star formation is the main cause of emission, as predicted by the radio-FIR correlation. This already shows that star-formation alone can not explain the spectral energy distribution.

The continuum emission shows a strong unresolved component at a resolution of 100 mas. At a redshift of 3.911, and assuming the cosmological parameters of $H_0 = 67.74 \text{ km/s Mpc}^{-1}$ and $\Omega_m = 0.3089$ (Planck Collaboration et al., 2016), one arcsecond corresponds to 7.18 kpc (Wright, 2006). Given that we have a resolution of ~ 100 mas, and a predicted magnification factor of $\mu_L = 4$ (Riechers et al., 2009), we find that the unresolved component can not be larger than 170 pc. Such a compact source of emission will most likely be the AGN. In addition, major parts of the CO emission appear to coincide with the peaks in the continuum emission. This is consistent with the prediction that the AGN is the main cause of emission at an observed frequency of 24 GHz.

The peak brightnesses of the individual images show deviations on the order of $2\text{-}\sigma$. While these deviations are not very strong, they are significant, and therefore they suggest a compact source of emission.

Chapter 6

Conclusion

The continuum emission of APM08279+5255 consists of a dominant unresolved component, and a weak extended component. By integrating the flux over the quasar, we derive a total flux density at a frequency of 23.9 GHz of $406 \pm 22 \mu\text{Jy}$. By fitting a power-law through the spectrum of the quasar, we derive a spectral index of -2.0 ± 0.3 . Also, we derive peak brightness ratios of $b(A, B) = 0.766 \pm 0.015$ and $b(A, C) = 0.561 \pm 0.014$. These brightness ratios agree with the expected brightness ratios fairly well, although there is slight deviation. This may suggest that the proposed lens model needs adjustment, but it could also point towards time variability of the source.

For the CO($J = 1 \rightarrow 0$) map, we find that the CO emission is mainly coincident with the continuum emission, apart from a structure to the west of the quasar. We derive a peak flux density of $216 \pm 28 \mu\text{Jy}$, and a full-width at half-maximum of $380 \pm 57 \text{ km/s}$. The peak flux density agrees with literature values, but the FWHM does not. The moment-1 map of the CO emission suggests that the molecular gas is rotating, but we do not find the map to be reliable enough to draw any conclusions.

The variations of the total flux density with time are insignificant, but the time variations of the peak brightnesses of the individual images do show deviations on the $2\text{-}\sigma$ level on a timescale of days. This suggests that part of the emission may come from the AGN, since only compact sources can give such rapid variability. However, we recognize that a $2\text{-}\sigma$ deviation is not enough to be sure.

The wide-field image of the environment of APM08279+5255 shows no detections of any other objects apart from one unresolved radio source $3''$ south of APM08279+5255. This radio source has been detected in earlier observations, but never at this frequency.

Finally, we conclude that a large part of the continuum emission of APM08279+5255 at an observed frequency of 23.9 GHz most likely originates from the AGN, but emission from star-formation activity is not excluded as a possibility.

Bibliography

- Condon, J. J. & Ransom, S. M. (2016). *Essential radio astronomy*. Princeton University Press.
- Högbom, J. A. (1974, June). Aperture synthesis with a non-regular distribution of interferometer baselines. *The Astrophysical Journal Supplement Series*, 15, 417–426.
- Ibata, R. A., Lewis, G. F., Irwin, M. J., Lehar, J., & Totten, E. J. (1999, November). NICMOS and VLA observations of the gravitationally lensed ultraluminous BAL quasar APM 08279+5255: Detection of a third image. *The Astronomical Journal*, 118(5), 1922–1930.
- Irwin, M. J., Ibata, R. A., Lewis, G. F., & Totten, E. J. (1998, October). Apm 08279+5255: an ultraluminous broad absorption line quasar at a redshift $z = 3.87$. *The Astrophysical Journal*, 505(2), 529–535.
- Ledoux, C., Theodore, B., Petitjean, P., Bremer, M. N., Lewis, G. F., Ibata, R. A., ... Totten, E. J. (1998, November). Adaptive optics imaging and integral field spectroscopy of APM 08279+5255: Evidence for gravitational lensing. *Astronomy and Astrophysics*, 339(3), L77–L80.
- Lewis, G. F., Ibata, R. A., Ellison, S. L., Aracil, B., Petitjean, P., Pettini, M., & Sri-anand, R. (2002, July). Spatially resolved STIS spectra of the gravitationally lensed broad absorption line quasar APM08279+5255: the nature of component C and evidence for microlensing. *Monthly Notices of the Royal Astronomical Society*, 334(1), L7–L10.
- Ott, J. & Kern, J. (2014, December 15). *CASA User Manual & Cookbook*. Retrieved from https://casa.nrao.edu/Release4.3/casa_cookbook.pdf
- Perley, R. A. & Butler, B. J. (2017, May). An Accurate Flux Density Scale from 50 MHz to 50 GHz. *The Astrophysical Journal Supplement Series*, 230(1), 7.
- Planck Collaboration, Ade, P. A. R., Aghanim, N., Arnaud, M., Ashdown, M., Aumont, J., ... et al. (2016, September). Planck 2015 results. XIII. Cosmological parameters. *Astronomy and Astrophysics*, 594, A13.
- Riechers, D. A., Walter, F., Carilli, C. L., Knudsen, K. K., Lo, K. Y., Benford, D. J., ... Scoville, N. Z. (2006, October). CO(1-0) in $z > 4$ Quasar Host Galaxies: No Evidence for Extended MOlecular Gas Reservoirs. *The Astrophysical Journal*, 650(2), 604–613.
- Riechers, D. A., Walter, F., Carilli, C. L., & Lewis, G. F. (2009, January). Imaging the molecular gas in a $z = 3.9$ quasar host galaxy at $0''.3$ arcsec: a central, sub-kiloparsec scale star formation reservoir in apm 08279+5255. *The Astrophysical Journal*, 690(1), 463–485.
- Stacey, H. R., McKean, J. P., Robertson, N. C., Ivison, R. J., Isaak, K. G., Schleicher, D. R. G., ... Loenen, E. (2017, May). Gravitational lensing reveals extreme dust-obscured star formation in quasar host galaxies. *ArXiv e-prints*. arXiv: [1705.10530](https://arxiv.org/abs/1705.10530)
- Wright, E. L. (2006, December). A Cosmology Calculator for the World Wide Web. *Astronomical Society of the Pacific*, 118, 1711–1715.

Appendix A

Images of observations

Here are the images of all 41 observations. Some images are better than others, but after thorough investigation we have to conclude that this can not be fixed. The problem most likely lies with the phases changing too quickly.

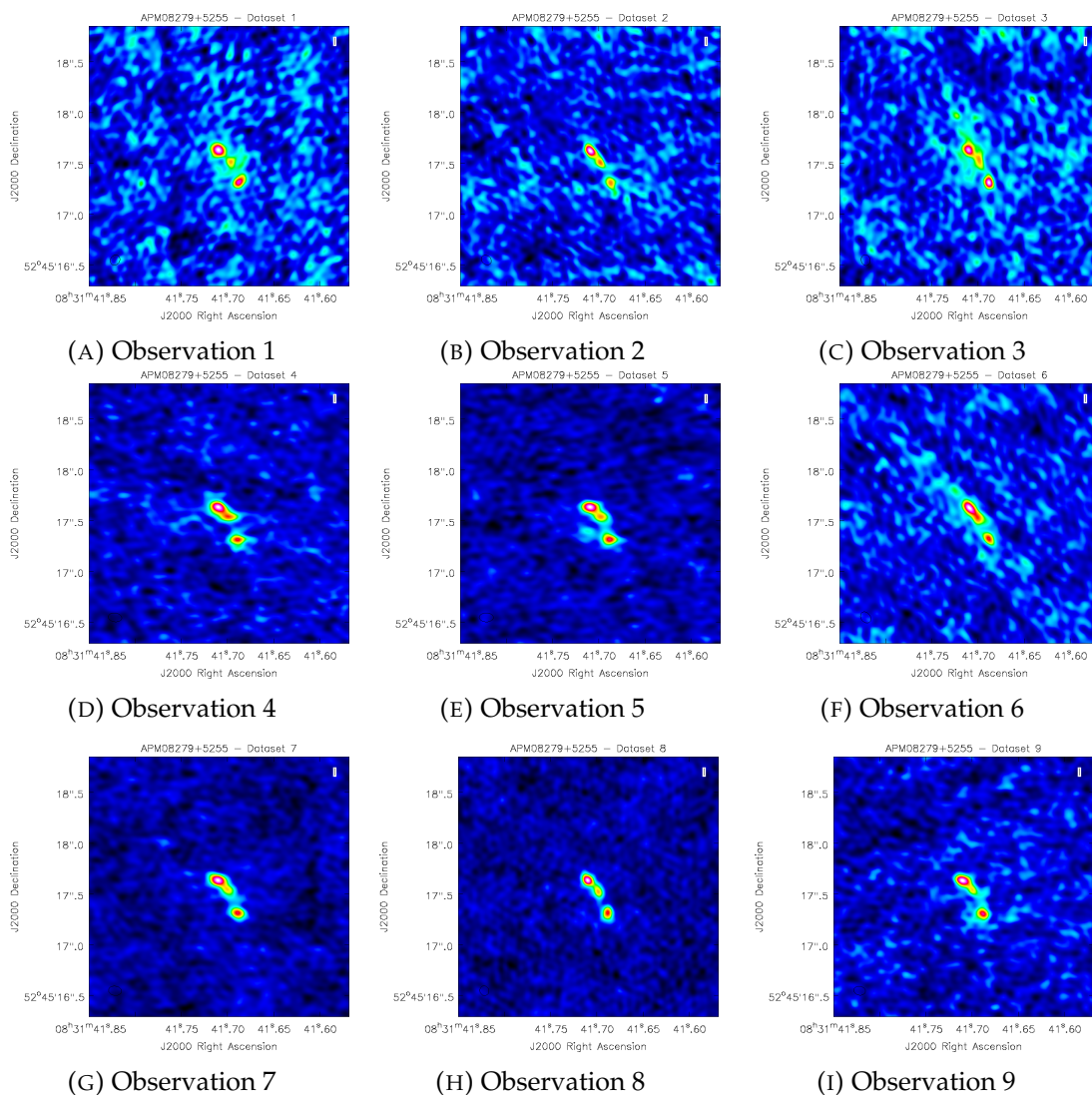


FIGURE A.1: Images of the individual observations

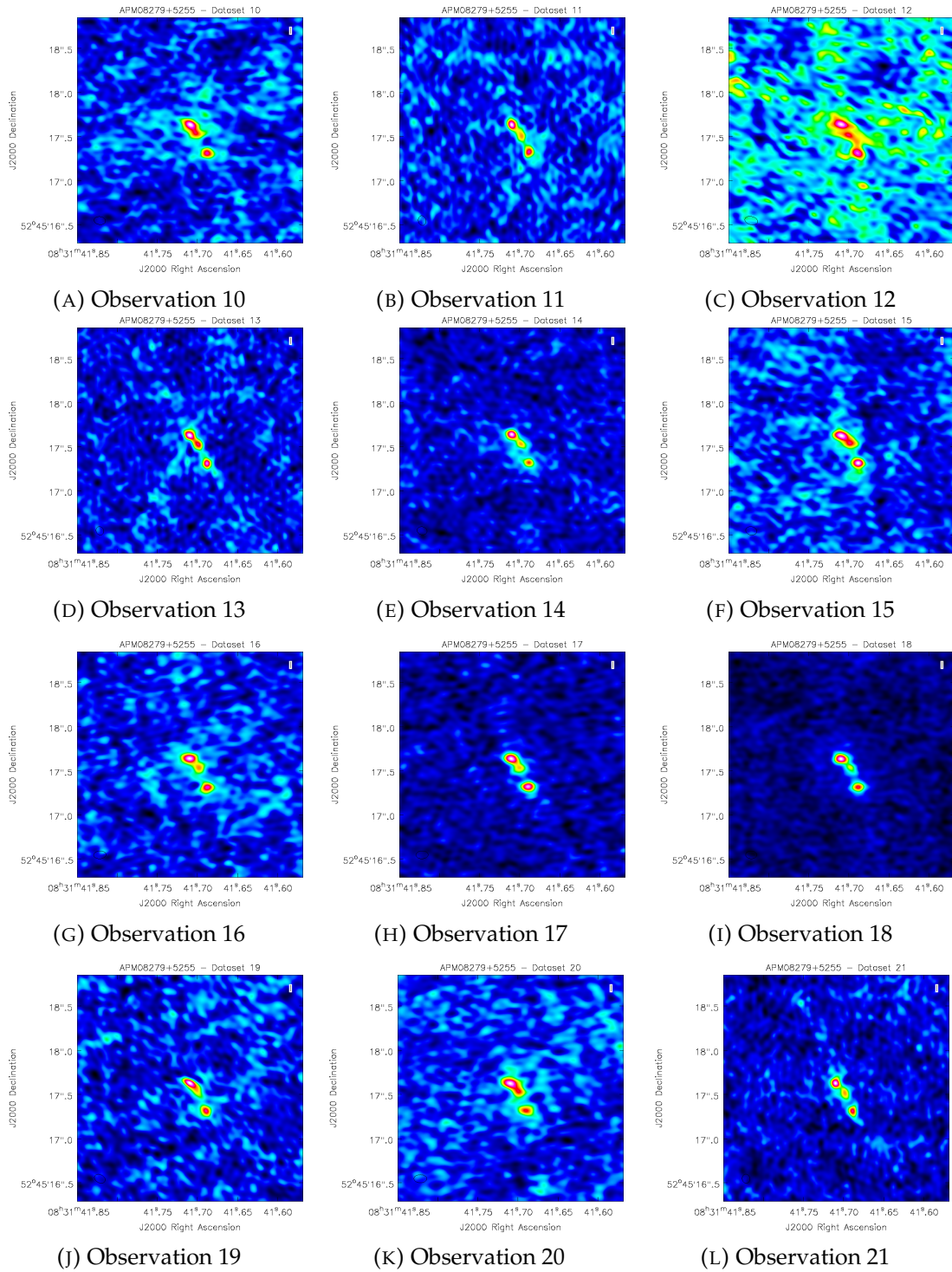


FIGURE A.2: Images of the individual observations

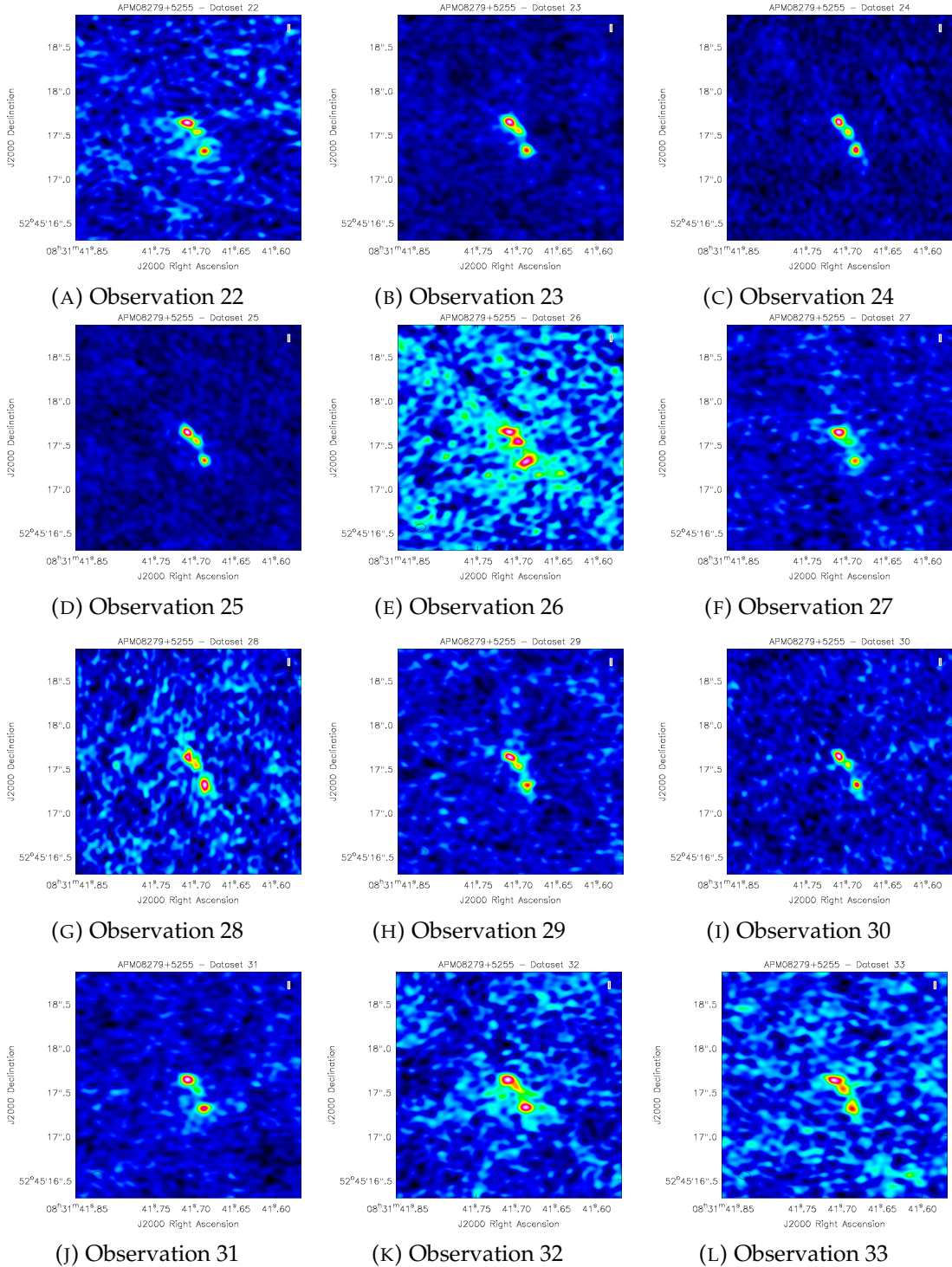


FIGURE A.3: Images of the individual observations

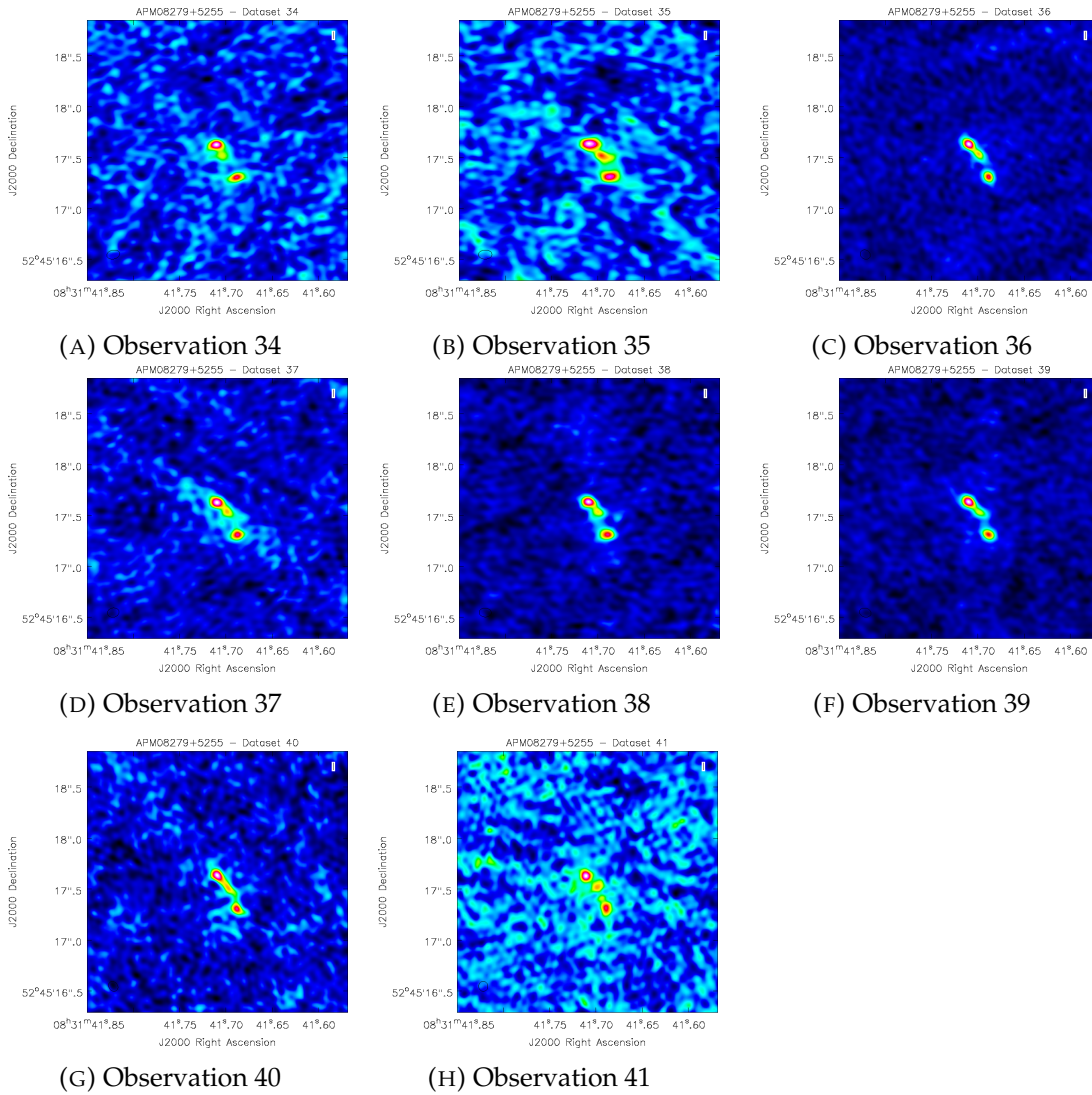


FIGURE A.4: Images of the individual observations

Appendix B

Python code

The following code was used to calibrate the datasets in CASA.

```

1 # JVLA data reduction script for APM08279+5255 (16 spws x 64
  # channels) in CASA 4.5.0
2 #
3 # Must be run with an internet connection to determine antenna
  # offsets and opacity measurements
4
5 #Calibration steps
6 thesteps = [0]
7 step_title = {0: 'Set the variables and initial split (split)',
8               1: 'A priori correction of opacity, antenna elevation
  # and antenna positions (gencal)',
9               2: 'Flag bad data (flagdata)',
10              3: 'Insert model of the flux calibrator (setjy)',
11              4: 'Short phase correction (gaincal)',
12              5: 'Delay correction (gaincal)',
13              6: 'Bandpass calibration (bandpass)',
14              7: 'Gain (Amplitude and Phase) calibration (gaincal)',
15              8: 'Determine the absolute flux-scale of the
  # calibrators (fluxscale)',
16              9: 'Applying the calibration tables (applycal)',
17              10: 'Split target (split)',
18              11: 'Clean and self-calibrate (phase) full dataset
  # (clean)'}
19
20 try:
21     print 'List of steps to be executed ...', mysteps
22     thesteps = mysteps
23 except:
24     print 'global variable mysteps not set.'
25 if (thesteps==[]):
26     thesteps = range(0,len(step_title))
27     print 'Executing all steps: ', thesteps
28
29
30 # The Python variable 'mysteps' will control which steps
31 # are executed when you start the script using
32 # execfile('scriptForCalibration.py')
33 # e.g. setting
34 # mysteps = [2,3,4]# before starting the script will make the
  # script execute
35 # only steps 2, 3, and 4
36 # Setting mysteps = [] will make it execute all steps.
37

```

```

38 print 'Write the value for variables and do a priori flagging ->
    run the script from the beginning'
39
40 #definitions
41 msfile = '12B-204.sb12419307.eb14032425.56257.30434325231.ms' #ms
    multisource file
42 myfield = '2,4,5' #fields to split
43 myspw = '0~15' #spw of interest
44 mssplit = '12B-204.D.ms' #ms file with the interesting sources
45 msscans = '12B-204.D.ms.txt' #text file to write listobs output to
46 mstarget = 'APM.D.ms' #ms file of the target
47 mstarget30s = 'APM.D.30s.ms'
48 myimage = 'APM.D.1'
49 mycube = 'APM.D.2.cube'
50 mytaperedcube = 'APM.D.1.t0.3cube'
51 mycontsub = 'APM.D.ms.contsub'
52 skymodel = 'APM.model'
53 mymask = 'APM.mask'
54 myrefant = 'ea05'
55 myplotants = 'plotants.png'
56 fluxfield = '0'
57 phasefield = '1'
58 targetfield = '2'
59
60
61 mystep = 0
62 if(mystep in thesteps):
63     casalog.post('Step '+str(mystep)+' '+step_title[mystep],'INFO')
64     print 'Step ', mystep, step_title[mystep]
65
66 # msfile = raw_input("Msfile, please: ")
67 # myfield = raw_input("Fields, please: ")
68 # myspw = raw_input("Spectral windows, please: ")
69 # mssplit = raw_input("Write the name of the mssplit file, please:
    ")
70 # myTau = raw_input("Opacity parameter, please: ")
71
72 split(vis=msfile, outputvis= mssplit, datacolumn="data",
    field=myfield, spw=myspw, width=1, antenna="", timebin="",
    timerange="", scan="", intent="", array="", uvrange="",
    correlation="rr, ll", observation="", combine="",
    keepflags=True, keepmms=False)
73
74 listobs(vis=mssplit, selectdata=True, spw="", field="",
    antenna="", uvrange="", timerange="", correlation="",
    scan="", intent="", feed="", array="", observation="",
    verbose=True, listfile=msscans, listunfl=False, cachesize=50,
    overwrite=True)
75
76 plotants(vis=msfile, figfile=myplotants)
77
78 plotuv(vis="12B-204.D.ms", field=fluxfield, antenna="", spw="",
    observation="", array="", maxnpts=10000000, colors=['r', 'y',
    'g', 'b'], symb="", "", ncycles=1,
    figfile="12B-204.D.3C147.uv.png")
79

```

```

80 plotuv(vis="12B-204.D.ms", field=phasefield, antenna="", spw="",
      observation="", array="", maxnpts=100000000, colors=['r',
      'y', 'g', 'b'], symb="", "", ncycles=1,
      figfile="12B-204.D.J0808+4950.uv.png")
81
82 plotuv(vis="12B-204.D.ms", field=targetfield, antenna="",
      spw="", observation="", array="", maxnpts=100000000,
      colors=['r', 'y', 'g', 'b'], symb="", "", ncycles=1,
      figfile="12B-204.D.APM08279+5255.uv.png")
83
84
85
86
87 # step a priori splitting and calibration
88 mystep = 1
89 if(mystep in thesteps):
90     casalog.post('Step '+str(mystep)+' '+step_title[mystep],'INFO')
91     print 'Step ', mystep, step_title[mystep]
92
93 myTau = plotweather(vis=mssplit, doPlot=T)
94
95 gencal(vis=mssplit, caltable="opacity.cal", caltype="opac",
      spw=myspw, antenna="", pol="", parameter=myTau)
96
97 gencal(vis=mssplit, caltable="antpos.cal", caltype="antpos",
      spw="", antenna="", pol="", parameter=[])
98
99 gencal(vis=mssplit, caltable="gaincurve.cal", caltype="gceff",
      spw="", antenna="", pol="", parameter=[])
100
101
102
103 # step flagging
104 mystep = 2
105 if(mystep in thesteps):
106     casalog.post('Step '+str(mystep)+' '+step_title[mystep],'INFO')
107     print 'Step ', mystep, step_title[mystep]
108
109 # pre-calibration flags
110 # plotms amp vs time/freq/uvdist
111
112 # flag zeros

```

```

113  flagdata(vis=mssplit, mode="clip", autocorr=False, infile="",
        reason="any", tbuff=0.0, spw="", field="", antenna="",
        uvrange="", timerange="", correlation="", scan="", intent="",
        array="", observation="", feed="", clipminmax=[],
        datacolumn="DATA", clipoutside=True, channelavg=False,
        clipzeros=True, quackinterval=1.0, quackmode="beg",
        quackincrement=False, tolerance=0.0, addantenna="",
        lowerlimit=0.0, upperlimit=90.0, ntime="scan",
        combinescans=False, timecutoff=4.0, freqcutoff=3.0,
        timefit="line", freqfit="poly", maxnpieces=7,
        flagdimension="freqtime", usewindowstats="none", halfwin=1,
        extendflags=True, winsize=3, timedev="", freqdev="",
        timedevscale=5.0, freqdevscale=5.0, spectralmax=1000000.0,
        spectralmin=0.0, extendpols=True, growtime=50.0,
        growfreq=50.0, growaround=False, flagneartime=False,
        flagnearfreq=False, minrel=0.0, maxrel=1.0, minabs=0,
        maxabs=-1, spwchan=False, spwcorr=False, basecnt=False,
        name="Summary", action="apply", display="", flagbackup=True,
        savepars=False, cmdreason="", outfile="")
114
115  flagdata(vis=mssplit, mode="manual", autocorr=False, infile="",
        reason="any", tbuff=0.0, spw="", field="", antenna="",
        uvrange="", timerange="5:22:43~5:22:44", correlation="",
        scan="", intent="", array="", observation="", feed="",
        clipminmax=[], datacolumn="DATA", clipoutside=True,
        channelavg=False, clipzeros=False, quackinterval=1.0,
        quackmode="beg", quackincrement=False, tolerance=0.0,
        addantenna="", lowerlimit=0.0, upperlimit=90.0, ntime="scan",
        combinescans=False, timecutoff=4.0, freqcutoff=3.0,
        timefit="line", freqfit="poly", maxnpieces=7,
        flagdimension="freqtime", usewindowstats="none", halfwin=1,
        extendflags=True, winsize=3, timedev="", freqdev="",
        timedevscale=5.0, freqdevscale=5.0, spectralmax=1000000.0,
        spectralmin=0.0, extendpols=True, growtime=50.0,
        growfreq=50.0, growaround=False, flagneartime=False,
        flagnearfreq=False, minrel=0.0, maxrel=1.0, minabs=0,
        maxabs=-1, spwchan=False, spwcorr=False, basecnt=False,
        name="Summary", action="apply", display="", flagbackup=True,
        savepars=False, cmdreason="", outfile="")
116
117  #.....
118
119  # step: model of the flux calibrator-setjy
120  # observation at 23.9 GHz, using K band model
121  mystep = 3
122  if(mystep in thesteps):
123      casalog.post('Step '+str(mystep)+' '+step_title[mystep], 'INFO')
124      print 'Step ', mystep, step_title[mystep]
125
126  setjy(vis=mssplit, field=fluxfield, spw="", selectdata=False,
        timerange="", scan="", intent="", observation="",
        scalebychan=True, standard="Perley-Butler 2010",
        model="3C147_K.im", modimage=None, listmodels=False,
        fluxdensity=-1, spix=0.0, reffreq="1GHz", polindex=[],
        rotmeas=0.0, fluxdict={}, useephemdir=False,
        interpolation="nearest", usescratch=True, ismms=None)
127

```

```

128
129 # step: short phase calibration
130 mystep = 4
131 if(mystep in thesteps):
132     casalog.post('Step '+str(mystep)+' '+step_title[mystep],'INFO')
133     print 'Step ', mystep, step_title[mystep]
134
135 gaincal(vis=mssplit, caltable="intphase.cal", field=fluxfield,
136         spw="*:28~36", intent="", selectdata=False, timerange="",
137         uvrange="", antenna="", scan="", observation="", msselect="",
138         solint="int", combine="", preavg=-1.0, refant=myrefant,
139         minblperant=4, minsnr=2.0, solnorm=False, gaintype="G",
140         smodel=[], calmode="p", append=False, splinetime=3600.0,
141         npointaver=3, phasewrap=180.0, docallib=False, callib="",
142         gaintable=['antpos.cal', 'gaincurve.cal', 'opacity.cal'],
143         gainfield=[], interp=[], spwmap=[], parang=False)
144
145
146
147
148 # step: residual delay calibration
149 mystep = 5
150 if(mystep in thesteps):
151     casalog.post('Step '+str(mystep)+' '+step_title[mystep],'INFO')
152     print 'Step ', mystep, step_title[mystep]
153
154 gaincal(vis=mssplit, caltable="delays.cal", field=fluxfield,
155         spw="", intent="", selectdata=False, timerange="",
156         uvrange="", antenna="", scan="", observation="", msselect="",
157         solint="inf", combine="scan", preavg=-1.0, refant=myrefant,
158         minblperant=4, minsnr=2.0, solnorm=False, gaintype="K",
159         smodel=[], calmode="p", append=False, splinetime=3600.0,
160         npointaver=3, phasewrap=180.0, docallib=False, callib="",
161         gaintable=['antpos.cal', 'gaincurve.cal', 'opacity.cal',
162                   'intphase.cal'], gainfield=[], interp=[], spwmap=[],
163         parang=False)
164
165
166
167
168 # step: bandpass calibration
169 mystep = 6
170 if(mystep in thesteps):
171     casalog.post('Step '+str(mystep)+' '+step_title[mystep],'INFO')
172     print 'Step ', mystep, step_title[mystep]
173
174 bandpass(vis=mssplit, caltable="bpass.cal", field=fluxfield,
175         spw="", intent="", selectdata=False, timerange="",
176         uvrange="", antenna="", scan="", observation="", msselect="",
177         solint="inf", combine="scan", refant=myrefant, minblperant=4,
178         minsnr=2.0, solnorm=False, bandtype="B", smodel=[],
179         append=False, fillgaps=0, degamp=3, degphase=3,
180         visnorm=False, maskcenter=0, maskedge=5, docallib=False,
181         callib="", gaintable=['antpos.cal', 'gaincurve.cal',
182                               'opacity.cal', 'intphase.cal', 'delays.cal'], gainfield=[],
183         interp=[], spwmap=[], parang=False)
184
185
186
187
188 # step: phase & amplitude calibration

```

```

159 mystep = 7
160 if(mystep in thesteps):
161     casalog.post('Step '+str(mystep)+' '+step_title[mystep],'INFO')
162     print 'Step ', mystep, step_title[mystep]
163
164     gaincal(vis=mssplit, caltable="phase.cal", field=fluxfield,
            spw="*:4~60", intent="", selectdata=False, timerange="",
            uvrange="", antenna="", scan="", observation="", msselect="",
            solint="int", combine="", preavg=-1.0, refant=myrefant,
            minblperant=4, minsnr=2.0, solnorm=False, gaintype="G",
            smodel=[], calmode="p", append=False, splinetime=3600.0,
            npointaver=3, phasewrap=180.0, docallib=False, callib="",
            gaintable=['antpos.cal', 'gaincurve.cal', 'opacity.cal',
            'delays.cal', 'bpass.cal'], gainfield=[], interp=[],
            spwmap=[], parang=False)
165     gaincal(vis=mssplit, caltable="phase.cal", field=phasefield,
            spw="*:4~60", intent="", selectdata=False, timerange="",
            uvrange="", antenna="", scan="", observation="", msselect="",
            solint="int", combine="", preavg=-1.0, refant=myrefant,
            minblperant=4, minsnr=2.0, solnorm=False, gaintype="G",
            smodel=[], calmode="p", append=True, splinetime=3600.0,
            npointaver=3, phasewrap=180.0, docallib=False, callib="",
            gaintable=['antpos.cal', 'gaincurve.cal', 'opacity.cal',
            'delays.cal', 'bpass.cal'], gainfield=[], interp=[],
            spwmap=[], parang=False)
166
167     gaincal(vis=mssplit, caltable="amp.cal", field=fluxfield,
            spw="*:4~60", intent="", selectdata=False, timerange="",
            uvrange="", antenna="", scan="", observation="", msselect="",
            solint="inf", combine="", preavg=-1.0, refant=myrefant,
            minblperant=4, minsnr=2.0, solnorm=False, gaintype="G",
            smodel=[], calmode="ap", append=False, splinetime=3600.0,
            npointaver=3, phasewrap=180.0, docallib=False, callib="",
            gaintable=['antpos.cal', 'gaincurve.cal', 'opacity.cal',
            'delays.cal', 'bpass.cal', 'phase.cal'], gainfield=['', '',
            '', '0', '0', '0'], interp=['', '', '', 'nearest', 'nearest',
            'nearest'], spwmap=[], parang=False)
168     gaincal(vis=mssplit, caltable="amp.cal", field=phasefield,
            spw="*:4~60", intent="", selectdata=False, timerange="",
            uvrange="", antenna="", scan="", observation="", msselect="",
            solint="inf", combine="", preavg=-1.0, refant=myrefant,
            minblperant=4, minsnr=2.0, solnorm=False, gaintype="G",
            smodel=[], calmode="ap", append=True, splinetime=3600.0,
            npointaver=3, phasewrap=180.0, docallib=False, callib="",
            gaintable=['antpos.cal', 'gaincurve.cal', 'opacity.cal',
            'delays.cal', 'bpass.cal', 'phase.cal'], gainfield=['', '',
            '', '0', '0', '1'], interp=['', '', '', 'nearest', 'nearest',
            'nearest'], spwmap=[], parang=False)
169
170
171
172 # step: absolute flux-scale calibration
173 mystep = 8
174 if(mystep in thesteps):
175     casalog.post('Step '+str(mystep)+' '+step_title[mystep],'INFO')
176     print 'Step ', mystep, step_title[mystep]
177

```

```

178 flux1 = fluxscale(vis=mssplit, caltable="amp.cal",
    fluxtable="flux.cal", reference=[fluxfield],
    transfer=[phasefield], listfile="", append=False,
    refspwmap=[-1], gainthreshold=-1.0, antenna="", timerange="",
    scan="", incremental=True, fitorder=1, display=True)
179
180 setjy(vis=mssplit, field=phasefield, spw="", selectdata=False,
    timerange="", scan="", intent="", observation="",
    scalebychan=True, standard="fluxscale", model="",
    modimage=None, listmodels=False, fluxdensity=-1, spix=0.0,
    reffreq="1GHz", polindex=[], polangle=[], rotmeas=0.0,
    fluxdict=flux1, useephemdir=False, interpolation="nearest",
    usescratch=True, ismms=None)
181
182 gaincal(vis=mssplit, caltable="intphase2.cal", field=phasefield,
    spw="*:28~36", intent="", selectdata=False, timerange="",
    uvrange="", antenna="", scan="", observation="", msselect="",
    solint="int", combine="", preavg=-1.0, refant=myrefant,
    minblperant=4, minsnr=2.0, solnorm=False, gaintype="G",
    smodel=[], calmode="p", append=False, splinetime=3600.0,
    npointaver=3, phasewrap=180.0, docallib=False, callib="",
    gaintable=['antpos.cal', 'gaincurve.cal', 'opacity.cal'],
    gainfield=[], interp=[], spwmap=[], parang=False)
183
184 gaincal(vis=mssplit, caltable="delays2.cal", field=phasefield,
    spw="", intent="", selectdata=False, timerange="",
    uvrange="", antenna="", scan="", observation="", msselect="",
    solint="inf", combine="scan", preavg=-1.0, refant=myrefant,
    minblperant=4, minsnr=2.0, solnorm=False, gaintype="K",
    smodel=[], calmode="p", append=False, splinetime=3600.0,
    npointaver=3, phasewrap=180.0, docallib=False, callib="",
    gaintable=['antpos.cal', 'gaincurve.cal', 'opacity.cal',
    'intphase2.cal'], gainfield=[], interp=[], spwmap=[],
    parang=False)
185
186 bandpass(vis=mssplit, caltable="bpass2.cal", field=phasefield,
    spw="", intent="", selectdata=False, timerange="",
    uvrange="", antenna="", scan="", observation="", msselect="",
    solint="inf", combine="scan", refant=myrefant, minblperant=4,
    minsnr=2.0, solnorm=False, bandtype="B", smodel=[],
    append=False, fillgaps=0, degamp=3, degphase=3,
    visnorm=False, maskcenter=0, maskedge=5, docallib=False,
    callib="", gaintable=['antpos.cal', 'gaincurve.cal',
    'opacity.cal', 'intphase2.cal', 'delays2.cal'], gainfield=[],
    interp=[], spwmap=[], parang=False)
187
188 gaincal(vis=mssplit, caltable="phase2.cal", field=phasefield,
    spw="*:4~60", intent="", selectdata=False, timerange="",
    uvrange="", antenna="", scan="", observation="", msselect="",
    solint="int", combine="", preavg=-1.0, refant=myrefant,
    minblperant=4, minsnr=2.0, solnorm=False, gaintype="G",
    smodel=[], calmode="p", append=True, splinetime=3600.0,
    npointaver=3, phasewrap=180.0, docallib=False, callib="",
    gaintable=['antpos.cal', 'gaincurve.cal', 'opacity.cal',
    'delays2.cal', 'bpass2.cal'], gainfield=[], interp=[],
    spwmap=[], parang=False)
189

```

```

190 gaincal(vis=mssplit, caltable="amp2.cal", field=phasefield,
        spw="*:4~60", intent="", selectdata=False, timerange="",
        uvrange="", antenna="", scan="", observation="", msselect="",
        solint="inf", combine="", preavg=-1.0, refant=myrefant,
        minblperant=4, minsnr=2.0, solnorm=False, gaintype="G",
        smodel=[], calmode="ap", append=False, splinetime=3600.0,
        npointaver=3, phasewrap=180.0, docallib=False, callib="",
        gaintable=['antpos.cal', 'gaincurve.cal', 'opacity.cal',
        'delays2.cal', 'bpass2.cal', 'phase2.cal'], gainfield=[],
        interp=['', '', '', 'nearest', 'nearest', 'nearest'],
        spwmap=[], parang=False)
191
192
193 # step: Application of the calibration tables
194 mystep = 9
195 if(mystep in thesteps):
196     casalog.post('Step '+str(mystep)+' '+step_title[mystep], 'INFO')
197     print 'Step ', mystep, step_title[mystep]
198
199 applycal(vis=mssplit, field=fluxfield, spw="", intent="",
        selectdata=False, timerange="", uvrange="", antenna="",
        scan="", observation="", msselect="", docallib=False,
        callib="", gaintable=['antpos.cal', 'gaincurve.cal',
        'opacity.cal', 'delays.cal', 'bpass.cal', 'phase.cal',
        'amp.cal'], gainfield=['', '', '', '0', '0', '0', '0'],
        interp=['', '', '', 'nearest', 'nearest', 'linear',
        'nearest'], spwmap=[], calwt=False, parang=False,
        applymode="", flagbackup=True)
200 applycal(vis=mssplit, field=phasefield, spw="", intent="",
        selectdata=False, timerange="", uvrange="", antenna="",
        scan="", observation="", msselect="", docallib=False,
        callib="", gaintable=['antpos.cal', 'gaincurve.cal',
        'opacity.cal', 'delays2.cal', 'bpass2.cal', 'phase2.cal',
        'amp2.cal'], gainfield=['', '', '', '1', '1', '1', '1'],
        interp=['', '', '', 'nearest', 'nearest', 'linear',
        'nearest'], spwmap=[], calwt=False, parang=False,
        applymode="", flagbackup=True)
201 applycal(vis=mssplit, field=targetfield, spw="", intent="",
        selectdata=False, timerange="", uvrange="", antenna="",
        scan="", observation="", msselect="", docallib=False,
        callib="", gaintable=['antpos.cal', 'gaincurve.cal',
        'opacity.cal', 'delays2.cal', 'bpass2.cal', 'phase2.cal',
        'amp2.cal'], gainfield=['', '', '', '1', '1', '1', '1'],
        interp=['', '', '', 'nearest', 'nearest', 'linear',
        'nearest'], spwmap=[], calwt=False, parang=False,
        applymode="", flagbackup=True)
202
203
204 # step: Split target
205 mystep = 10
206 if(mystep in thesteps):
207     casalog.post('Step '+str(mystep)+' '+step_title[mystep], 'INFO')
208     print 'Step ', mystep, step_title[mystep]
209

```

```

210 split(vis=mssplit, outputvis=mstarget, datacolumn="corrected",
        field=targetfield, spw="", width=1, antenna="", timebin="",
        timerange="", scan="", intent="", array="", uvrange="",
        correlation="", observation="", combine="", keepflags=True,
        keepmms=False)
211 split(vis=mssplit, outputvis=mstarget30s,
        datacolumn="corrected", field=targetfield, spw="", width=1,
        antenna="", timebin="30s", timerange="", scan="", intent="",
        array="", uvrange="", correlation="", observation="",
        combine="", keepflags=True, keepmms=False)
212
213
214 # step: Clean full dataset for z = 3.911
215 mystep = 11
216 if(mystep in thesteps):
217     casalog.post('Step '+str(mystep)+' '+step_title[mystep],'INFO')
218     print 'Step ', mystep, step_title[mystep]
219
220 clean(vis=mstarget30s, imagename="12B-204.D.clean",
        outlierfile="", field="", spw="0~15:6~58", selectdata=True,
        timerange="", uvrange="", antenna="", scan="",
        observation="", intent="", mode="mfs", resmooth=False,
        gridmode="", wprojplanes=-1, facets=1, cfcache="cfcache.dir",
        rotpainc=5.0, painc=360.0, aterm=True, psterm=False,
        mterm=True, wbawp=False, conjbeams=True, epjtable="",
        interpolation="linear", niter=10000, gain=0.05,
        threshold="0.03mJy", psfmode="clark", imagermode="csclean",
        ftmachine="mosaic", mosweight=False, scaletype="SAULT",
        multiscale=[], negcomponent=-1, smallscalebias=0.6,
        interactive=True, mask=[], nchan=-1, start=0, width=1,
        outframe="", veltype="radio", imsize=[128, 128],
        cell=['0.02arcsec', '0.02arcsec'], phasecenter="",
        restfreq="", stokes="I", weighting="natural", robust=0,
        uvtaper=False, outertaper=[''], innertaper=['1.0'],
        modelimage="", restoringbeam=[''], pbcor=False, minpb=0.2,
        usescratch=True, noise="1.0Jy", npixels=0, npercycle=100,
        cyclefactor=1.5, cyclespeedup=-1, nterms=1, reffreq="",
        chaniter=False, flatnoise=True, allowchunk=False)
221
222 print 'Calibration and imaging completed'

```
